Petrogenesis of late triassic high-silica granites in the North Qiangtang terrane, central Tibetan Plateau

Changjun Ji[1], Bin Liu[2]*, Yun Chen[1], Zhenhan Wu[1] and Chong Chen[3]

[1]Chinese Academy of Geological Sciences, Beijing, China, [2]School of Geosciences, Yangtze University, Wuhan, China, [3]No. 6 Geological Party, Xizang Bureau of Geology and Mineral Exploration and Development, Lhasa, China

Although high-silica granites can provide unique insights into the maturity of the continental crust and rare metal enrichment, the origin of high-silica granitic magmatism remains uncertain. In this paper, we present an integrated study of zircon U-Pb geochronology and trace elements, whole-rock geochemistry, and Sr-Nd isotopes for two typical high-silica granites (namely, the Longbao granitic porphyry and the Yushu granite) found in the North Qiangtang terrane, central Tibetan Plateau. Zircon geochronological data indicate that these high-silica granites crystallized at 217–214 Ma. All the samples from the Longbao granitic porphyry and the Yushu granite exhibited high SiO_2, low MgO, depletion of Ba, Nb, Sr, P, and Ti, and enrichment of Th and U. They exhibited relatively high $(^{87}Sr/^{86}Sr)_i$ ratios of 0.7120–0.7136 and low $\varepsilon_{Nd}(t)$ values of $-8.58 \sim -7.58$; together with their old ages according to the two-stage Nd model (1.6–1.7 Ga), these features indicate the involvement of crustal materials. Geochemical and isotopic variation indicated that the high-silica granites studied were mainly produced by the dehydration melting of a muscovite (Ms)-bearing source, and that the Triassic turbidites might be a good candidate for the magma source. Combining this evidence with new regional studies, it can be concluded that partial melting of Triassic turbidites induced by slab roll-back might be the key factor controlling the origin of Late Triassic magmatism in the North Qiangtang terrane.

KEYWORDS

high-silica granites, crustal melting, triassic turbidites, north qiangtang, central Tibetan Plateau

1 Introduction

One of the distinguishing features that sets Earth apart from other planets in our Solar System and renders it able to sustain life is the felsic continental crust (Brown, 2013; Keller et al., 2015), and granitoids are essential for the formation of Earth's stable continental crust (Campbell and Taylor, 1983). High-silica granite (SiO_2>70 wt%) is a unique rock type among the granitoids found on Earth, and can serve as a valuable indicator of the compositional maturity of continental crust (Glazner et al., 2008; Lee and Morton, 2015; Wu et al., 2017). High-silica granites are enriched in incompatible elements (such as Li, Be, Nb, Ta, Zr, and Hf) and are closely associated with rare-metal mineralization (Wu et al., 2020; Shuai et al., 2021; Deng et al.,
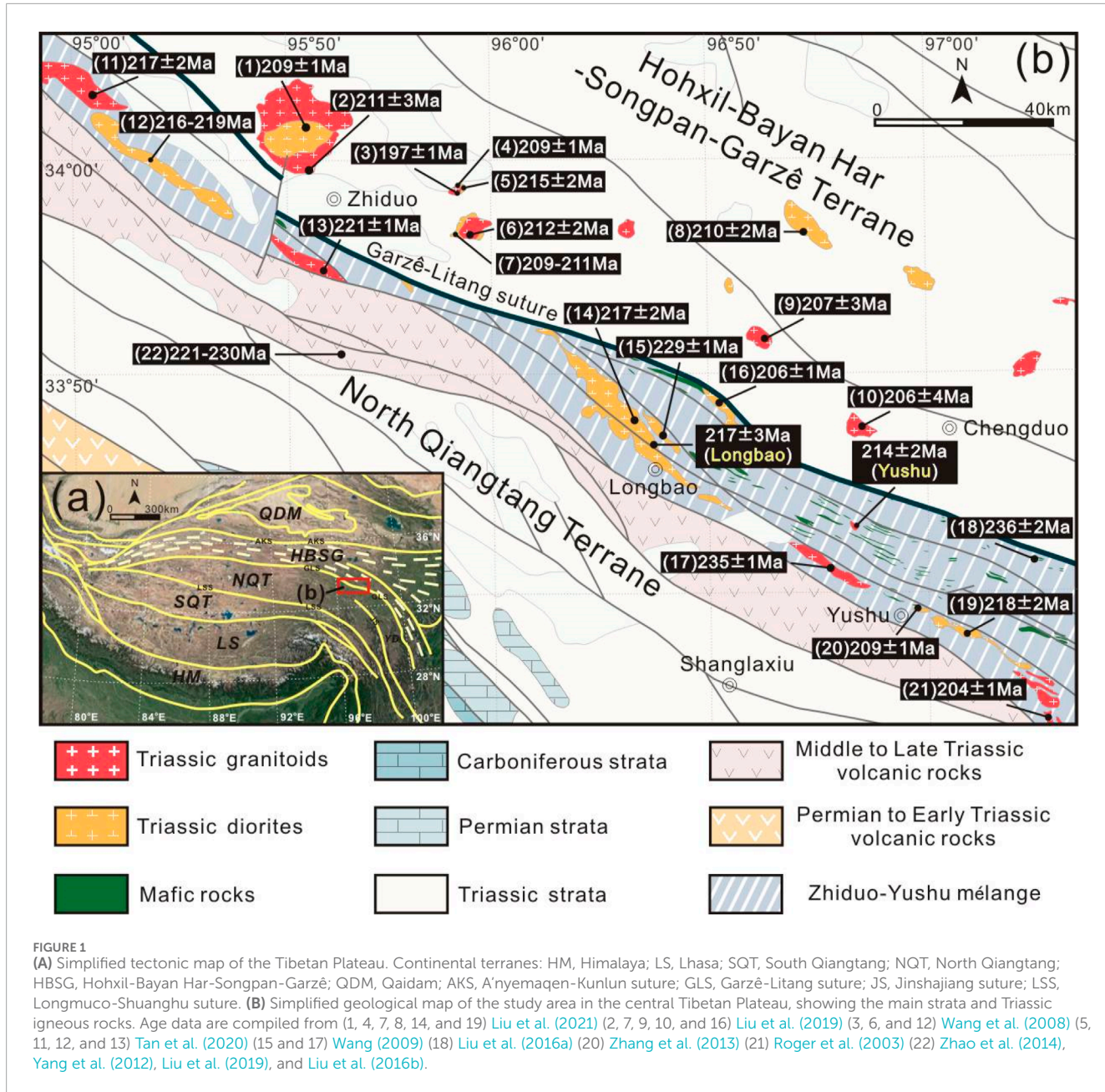
FIGURE 1
(A) Simplified tectonic map of the Tibetan Plateau. Continental terranes: HM, Himalaya; LS, Lhasa; SQT, South Qiangtang; NQT, North Qiangtang; HBSG, Hohxil-Bayan Har-Songpan-Garzê; QDM, Qaidam; AKS, A'nyemaqen-Kunlun suture; GLS, Garzê-Litang suture; JS, Jinshajiang suture; LSS, Longmuco-Shuanghu suture. **(B)** Simplified geological map of the study area in the central Tibetan Plateau, showing the main strata and Triassic igneous rocks. Age data are compiled from (1, 4, 7, 8, 14, and 19) Liu et al. (2021) (2, 7, 9, 10, and 16) Liu et al. (2019) (3, 6, and 12) Wang et al. (2008) (5, 11, 12, and 13) Tan et al. (2020) (15 and 17) Wang (2009) (18) Liu et al. (2016a) (20) Zhang et al. (2013) (21) Roger et al. (2003) (22) Zhao et al. (2014), Yang et al. (2012), Liu et al. (2019), and Liu et al. (2016b).

2022). However, the origin of high-silica granitic magmatism is uncertain. Previous studies have proposed various genetic models, including melting of metasedimentary or granitic rocks (e.g., Glazner et al., 2008; Frost et al., 2016), fractional crystallization (Lee and Morton, 2015), melt-crystal segregation (e.g., Chen et al., 2021), and magmatic-fluid interaction (Ballouard et al., 2016). Zircon is an accessory mineral widely occurring in felsic igneous rocks, and could play a crucial role in precisely recording the geological age, magma temperature, and long-term evolution of the silicic magma system (e.g., Zhu et al., 2023; Miller et al., 2003).

The Tibetan Plateau has generally been recognized as a natural laboratory for study of the Tethyan tectonic–magmatic evolution, mineralization, and continental dynamics (Xu et al., 2015). The central Tibetan Plateau is characterized by the development of the Palaeo-Tethyan orogenic system, which is

composed of multiple suture zones and terranes, high-pressure metamorphic belts, and island arc groups (Xu et al., 2015). With the tectonic evolution of the Palaeo-Tethyan Ocean, Triassic intermediate-acidic magmatic rocks were widespread in the central Tibetan Plateau. However, lively debate continues on the origin, petrogenesis, and geodynamic mechanisms of these magmatic rocks. For example, there is debate as to whether the Triassic granitic magmatism was derived from the melting of the Precambrian basement materials or related to the melting of the Hohxil-Bayan Har-Songpan-Garzê (HBSG) turbidites (Liu et al., 2021; Liu et al., 2023). There are still two competing models, a "collision-related" model and a "subduction-related" model, put forward to describe the Triassic tectonic evolution of the North Qiangtang terrane and the adjacent HBSG terrane (Yuan et al., 2010; Liu et al., 2021).
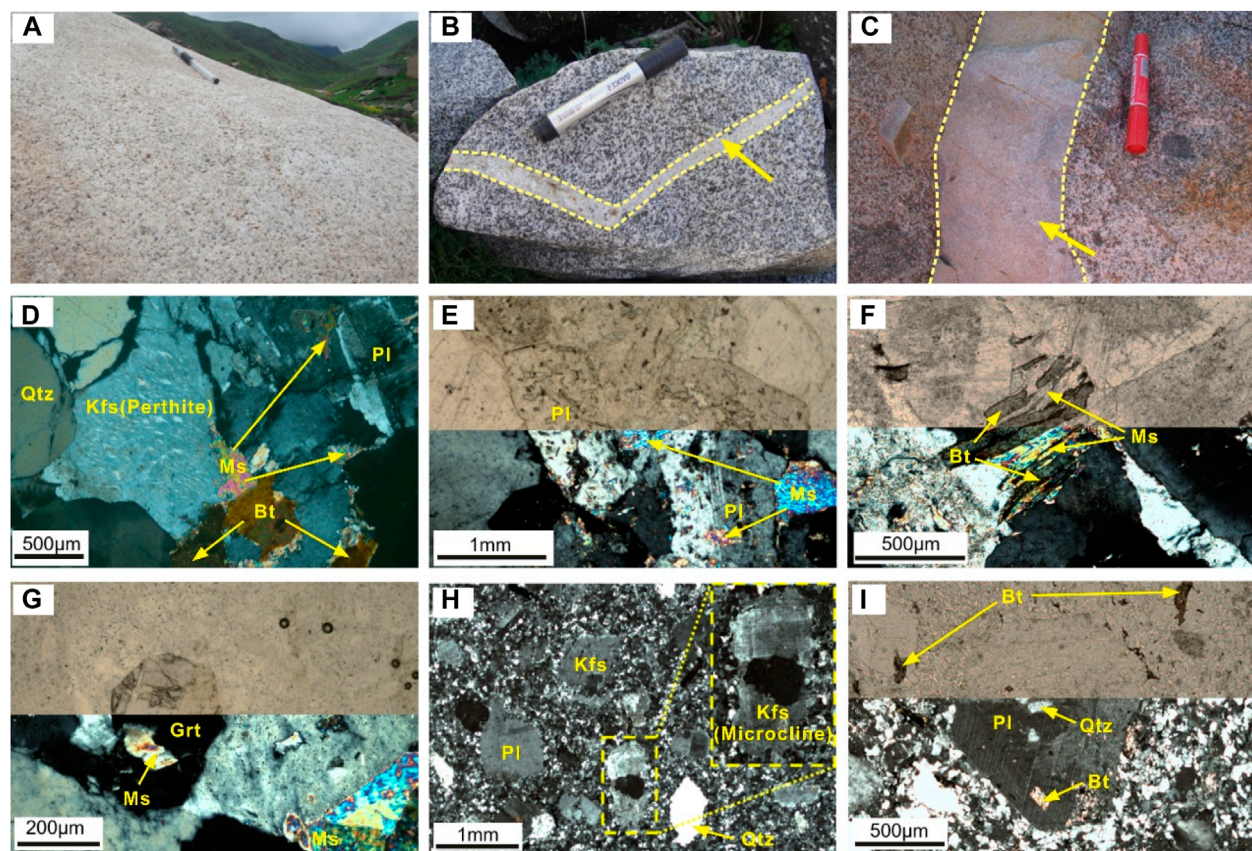
FIGURE 2
Field photographs and microscope photographs for **(A,D−G)** the Yushu granite and **(B,C and H,I)** the Longbao granitic porphyry. The upper halves of the microscope photographs (e, f, g, and **(I)** show images obtained with plane-polarized light, and the bottom halves, images obtained with perpendicular polarized light. Mineral abbreviations: Qtz, quartz; Kfs, K-feldspar; Pl, plagioclase; Bt, biotite; Ms, muscovite; Grt, garnet.

In this study, we present a comprehensive study of zircon U-Pb geochronology, zircon trace elements, whole-rock geochemistry, and Sr-Nd isotopes for two suites of newly identified high-silica granites in the central Tibetan Plateau. Those new results are used to constrain the petrogenesis of the Late Triassic high-silica granites, to reveal the Triassic crustal melting, and to further understand the geodynamic relationships of these granites with the Palaeo-Tethyan Ocean.

2 Geological background and sample description

There are four main Palaeo-Tethyan sutures in the central Tibetan Plateau, namely, from north to south, the A'nyemaqen-Kunlun suture, the Garzê-Litang suture, the Jinshajiang suture, and the Longmuco-Shuanghu suture. The HBSG terrane appears as an inverted triangular structure, from which the vast Triassic deep marine turbidites develop (Figure 1A; de Sigoyer et al., 2014). This voluminous series of turbidites are dominantly derived from the Dabie ultrahigh-pressure metamorphic rocks, the Qingling-Dabie orogen, the Kunlun arc, the South China terrane, or the Central Qiangtang ultrahigh-pressure metamorphic rocks (Weislogel et al.,

2006; Zhang et al., 2012; Ding et al., 2013; Jian et al., 2019; Chen et al., 2023). Late Triassic to Early Jurassic magmatic rocks are widespread in the HBSG terrane, and mainly include granitoids, minor diorites, and volcanic rocks (Liu et al., 2021). The NQ terrane consists of Paleozoic to Mesozoic sedimentary rocks, carbonate rocks, and interbedded volcanic rocks, and is underlain by the Precambrian crystalline basement, with ages of 991–1,044 Ma (He et al., 2013). With the southward subduction of the Garzê-Litang Paleo-Tethyan Ocean, Triassic volcanic rocks, diorites, and granitoids are linearly distributed along the northern margin of the NQ terrane (Liu et al., 2016a; Liu et al., 2016b; Liu et al., 2021; Liu et al., 2022; Tan et al., 2020; Yang et al., 2012).

In this study, we investigated two different suites of typical Late Triassic granitic rocks developed in the northern margin of the NQ terrane, which are represented by the Yushu granite and the Longbao granitic porphyry (Figure 1). The Yushu granite intrudes into the Zhiduo-Yushu mélange, with an exposed area of ~1.56 km². This pluton shows medium-to coarse-grained granular textures, and its granularity increases from the edge to the center (Figure 2A). The Yushu granite is composed of quartz (30%–38%), K-feldspar (30%–35%), plagioclase (15%–25%), muscovite (3%–5%), biotite (2%–4%), and minor accessory minerals including garnet, apatite, zircon, and opaque minerals. Most of the K-feldspar grains are

FIGURE 3
Representative cathodoluminescence and transmitted light images of zircons from the Longbao granitic porphyry **(A)** and the Yushu granite **(B, B1, B2)** samples. The corresponding ages, trace element concentrations, and elemental ratios are presented below the CL images. Yellow circles denote the positions of analysis of LA-ICP-MS for the U-Pb isotope, with spot size of 32 μm.

generally coarse-grained perthites, and their inclusions consist of plagioclase, quartz, and muscovite (Figure 2D). Plagioclase occurs as subhedral crystals, and exhibits some alterations by secondary muscovite (Figure 2E). Flaky muscovite and biotite occur as subhedral to anhedral crystals, and they are partly replaced by a small amount of chlorite (Figures 2D–G). Garnet shows euhedral or subhedral grain with minor muscovite inclusions (Figure 2G).

The Longbao granitic porphyry intrudes as dykes into the host diorite pluton and shows obvious chilled margins (Figures 2B, C). This granitic porphyry consists of phenocrysts (35%–40%) and matrixes (60%–65%). The phenocrysts mainly contain subhedral to xenomorphic fine-grained quartz (~30%), K-feldspar (~35%), plagioclase (~32%), and biotite (~3%). Some quartz phenocrysts show the dissolution harbor (Figure 2H). K-feldspar phenocrysts mainly contain microcline and orthoclase (Figure 2H). Plagioclase phenocrysts display typical polysynthetic twinning, and contain some quartz and biotite inclusions (Figure 2I). The matrixes are composed of the feldspar-quartz microcrystals and some cryptocrystalline substance (Figure 2H).

3 Methods

3.1 Zircon U-Pb dating and trace element composition

The selection of typical samples HX06-2 (Longbao) and RN03-1 (Yushu) for U-Pb isotopic dating was based on petrographic observations. Zircon grains were separated by conventional heavy liquid and magnetic methods and then purified under a binocular microscope. Cathodoluminescence (CL) images illustrate the internal morphology of the analyzed zircon grains (Figure 3). Zircon U-Pb geochronology analyses were conducted synchronously by LA-ICP-MS at the State Key Laboratory of Geological Processes and Mineral Resources (GPMR), China University of Geosciences, Wuhan. The details of instrument operating conditions and data processing can be found in Liu et al. (2010). Uncertainties for individual analyses are quoted at the 1 sigma level, and errors for weighted mean ages are quoted at 95% confidence. A common Pb correction was applied using the method described by Andersen (2002). Weighted mean $^{206}Pb/^{238}U$ ages were calculated and plotted using the ISOPLOT software.

3.2 Whole-rock geochemistry and Sr-Nd isotopes

The whole-rock major element analyses were performed at the Analytical Institute of the Bureau of Geology and Mineral Resources, Hubei Province, China. The analytical precision of the spectrometer employed was better than 5%. Trace elements were measured using an Agilent 7500a ICP-MS instrument at the GPMR, following the methods of Liu et al. (2008). The samples were digested with a mixture of HF + HNO_3 for ICP-MS analyses.

Whole-rock Sr-Nd isotopic compositions were determined using a Thermo-type Neptune Plus MC-ICP-MS instrument at the GPMR. Mass fractionation corrections for the isotopic ratios were based on $^{88}Sr/^{86}Sr = 8.375209$ and $^{146}Nd/^{144}Nd = 0.721900$. The JNdi-1 and NBS 987 standards were measured at a mean $^{88}Sr/^{86}Sr$

TABLE 1 LA-ICP-MS zircon U-Pb data for the Longbao granitic porphyry (HX06-2) and the Yushu granite (RN03-2), central Tibetan Plateau.

| Spot No.	Concentration (ppm)		Th/U	Isotopic ratios						Isotopic ages (Ma)					
	Th	U		$^{207}Pb/^{206}Pb$	±1σ	$^{207}Pb/^{235}U$	±1σ	$^{206}Pb/^{238}U$	±1σ	$^{207}Pb/^{206}Pb$	±1σ	$^{207}Pb/^{235}U$	±1σ	$^{206}Pb/^{238}U$	±1σ
HX06-2															
1	547	1,031	0.5	0.0585	0.0024	0.7556	0.0314	0.0942	0.0018	548	58	571	18	580	10
2	240	563	0.4	0.0535	0.0072	0.2825	0.0377	0.0383	0.0008	349	306	253	30	242	5
3	209	439	0.5	0.0461	0.0038	0.2128	0.0173	0.0335	0.0006		183	196	14	212	4
4	155	340	0.5	0.0553	0.0057	0.2563	0.0259	0.0336	0.0007	424	237	232	21	213	5
5	181	471	0.4	0.0494	0.0064	0.2452	0.0314	0.0360	0.0007	165	269	223	26	228	5
6	253	567	0.4	0.0518	0.0034	0.2496	0.0157	0.0356	0.0008	274	106	226	13	225	5
7	489	719	0.7	0.0527	0.0031	0.2520	0.0152	0.0344	0.0006	316	104	228	12	218	4
8	143	386	0.4	0.0658	0.0049	0.3030	0.0229	0.0340	0.0008	801	118	269	18	216	5
9	575	1,033	0.6	0.0510	0.0043	0.2394	0.0201	0.0341	0.0005	239	195	218	16	216	3
10	349	676	0.5	0.0544	0.0034	0.2585	0.0157	0.0351	0.0006	386	105	233	13	222	4
11	296	737	0.4	0.0516	0.0082	0.2622	0.0415	0.0369	0.0007	268	326	236	33	233	4
12	153	335	0.5	0.0696	0.0052	0.3136	0.0206	0.0348	0.0008	915	96	277	16	220	5
13	612	1,192	0.5	0.0505	0.0025	0.2551	0.0125	0.0367	0.0005	220	89	231	10	232	3
14	220	437	0.5	0.0489	0.0151	0.2332	0.0716	0.0346	0.0009	142	521	213	59	219	5
15	198	458	0.4	0.0680	0.0055	0.3088	0.0237	0.0343	0.0008	868	123	273	18	217	5
16	201	454	0.4	0.0493	0.0049	0.2307	0.0221	0.0340	0.0008	162	221	211	18	215	5
17	470	1830	0.3	0.0675	0.0051	1.0331	0.0770	0.1111	0.0015	852	162	720	38	679	8
18	290	921	0.3	0.0586	0.0022	0.7741	0.0305	0.0953	0.0014	551	60	582	17	587	8
19	684	2,254	0.3	0.0748	0.0018	1.7256	0.0420	0.1658	0.0019	1,062	31	1,018	16	989	10
20	392	578	0.7	0.0679	0.0025	1.1761	0.0444	0.1249	0.0018	866	54	790	21	759	10

TABLE 1 (*Continued*) LA-ICP-MS zircon U-Pb data for the Longbao granitic porphyry (HX06-2) and the Yushu granite (RN03-2), central Tibetan Plateau.

Spot No.	Concentration (ppm)		Th/U	Isotopic ratios						Isotopic ages (Ma)					
	Th	U		$^{207}Pb/^{206}Pb$	±1σ	$^{207}Pb/^{235}U$	±1σ	$^{206}Pb/^{238}U$	±1σ	$^{207}Pb/^{206}Pb$	±1σ	$^{207}Pb/^{235}U$	±1σ	$^{206}Pb/^{238}U$	±1σ
RN03-2															
1	542	2,379	0.2	0.0517	0.0028	0.2416	0.0126	0.0339	0.0005	270	127	220	10	215	3
2	613	1,289	0.5	0.0521	0.0065	0.2345	0.0289	0.0327	0.0006	289	282	214	24	207	4
3	675	1835	0.4	0.0488	0.0027	0.2392	0.0125	0.0354	0.0005	137	93	218	10	224	3
4	4,454	33,865	0.1	0.0557	0.0016	0.2507	0.0073	0.0320	0.0003	439	47	227	6	203	2
5	459	1834	0.3	0.0519	0.0026	0.2581	0.0135	0.0354	0.0006	282	87	233	11	225	4
6	2019	5,029	0.4	0.0517	0.0018	0.2565	0.0086	0.0357	0.0005	271	50	232	7	226	3
7	1,248	2,386	0.5	0.0539	0.0033	0.2475	0.0150	0.0333	0.0004	365	143	225	12	211	2
8	420	1,243	0.3	0.0535	0.0031	0.2813	0.0158	0.0383	0.0006	351	100	252	13	242	4
9	586	1,499	0.4	0.0474	0.0077	0.2158	0.0346	0.0330	0.0006	69	296	198	29	209	4
10	897	1831	0.5	0.0552	0.0027	0.2924	0.0143	0.0381	0.0006	421	84	260	11	241	3
11	2,898	24,917	0.1	0.0507	0.0027	0.2216	0.0115	0.0317	0.0004	228	125	203	10	201	3
12	736	5,294	0.1	0.0502	0.0017	0.2346	0.0075	0.0337	0.0005	206	47	214	6	214	3
13	684	1,235	0.6	0.0501	0.0028	0.2286	0.0124	0.0335	0.0005	200	97	209	10	212	3
14	1842	15,565	0.1	0.0518	0.0027	0.2448	0.0123	0.0343	0.0004	277	120	222	10	217	2
15	2,848	9,708	0.3	0.0513	0.0014	0.2987	0.0084	0.0418	0.0006	254	40	265	7	264	3
16	1,139	2,682	0.4	0.0499	0.0019	0.2419	0.0093	0.0349	0.0005	192	64	220	8	221	3
17	3,185	33,501	0.1	0.0512	0.0019	0.2264	0.0079	0.0321	0.0003	248	86	207	7	204	2
18	649	1815	0.4	0.0461	0.0032	0.2173	0.0146	0.0342	0.0004		151	200	12	217	3

TABLE 1 (*Continued*) LA-ICP-MS zircon U-Pb data for the Longbao granitic porphyry (HX06-2) and the Yushu granite (RN03-2), central Tibetan Plateau.

Spot No.	Concentration (ppm)		Th/U	Isotopic ratios						Isotopic ages (Ma)					
	Th	U		$^{207}Pb/^{206}Pb$	±1σ	$^{207}Pb/^{235}U$	±1σ	$^{206}Pb/^{238}U$	±1σ	$^{207}Pb/^{206}Pb$	±1σ	$^{207}Pb/^{235}U$	±1σ	$^{206}Pb/^{238}U$	±1σ
19	2,147	11,179	0.2	0.0545	0.0032	0.2743	0.0158	0.0365	0.0004	390	135	246	13	231	2
20	565	1817	0.3	0.0525	0.0025	0.2576	0.0127	0.0354	0.0005	309	85	233	10	224	3
21	719	1845	0.4	0.0530	0.0024	0.2763	0.0120	0.0378	0.0006	328	70	248	10	239	4
22	701	1,456	0.5	0.0964	0.0105	0.6211	0.0659	0.0467	0.0011	1,556	212	491	41	294	7
23	2067	6,032	0.3	0.0536	0.0040	0.2345	0.0172	0.0317	0.0005	356	172	214	14	201	3
24	6,072	29,337	0.2	0.0567	0.0015	0.2532	0.0069	0.0322	0.0004	478	39	229	6	204	2
25	1,290	2,107	0.6	0.0554	0.0026	0.2578	0.0122	0.0337	0.0005	427	79	233	10	214	3
26	7,143	22,880	0.3	0.0504	0.0030	0.2149	0.0123	0.0309	0.0004	213	136	198	10	196	2
27	2,549	12,166	0.2	0.0563	0.0054	0.2895	0.0276	0.0373	0.0004	465	219	258	22	236	2
28	2,524	17,790	0.1	0.0530	0.0035	0.2249	0.0145	0.0308	0.0004	327	153	206	12	196	3
29	465	3,032	0.2	0.0564	0.0035	0.3801	0.0233	0.0489	0.0006	467	143	327	17	308	4
30	1,455	17,739	0.1	0.0509	0.0024	0.2257	0.0102	0.0322	0.0005	234	112	207	8	204	3
31	3,603	21,823	0.2	0.0515	0.0029	0.2951	0.0145	0.0416	0.0011	263	131	263	11	263	7
32	1847	12,835	0.1	0.0531	0.0038	0.2621	0.0184	0.0358	0.0006	334	166	236	15	227	3
33	2,562	29,241	0.1	0.0511	0.0034	0.2180	0.0143	0.0310	0.0003	244	153	200	12	197	2
34	3,077	26,945	0.1	0.0535	0.0045	0.2293	0.0188	0.0311	0.0005	351	191	210	16	197	3
35	8,600	30,806	0.3	0.0507	0.0011	0.2212	0.0045	0.0314	0.0002	228	33	203	4	199	1
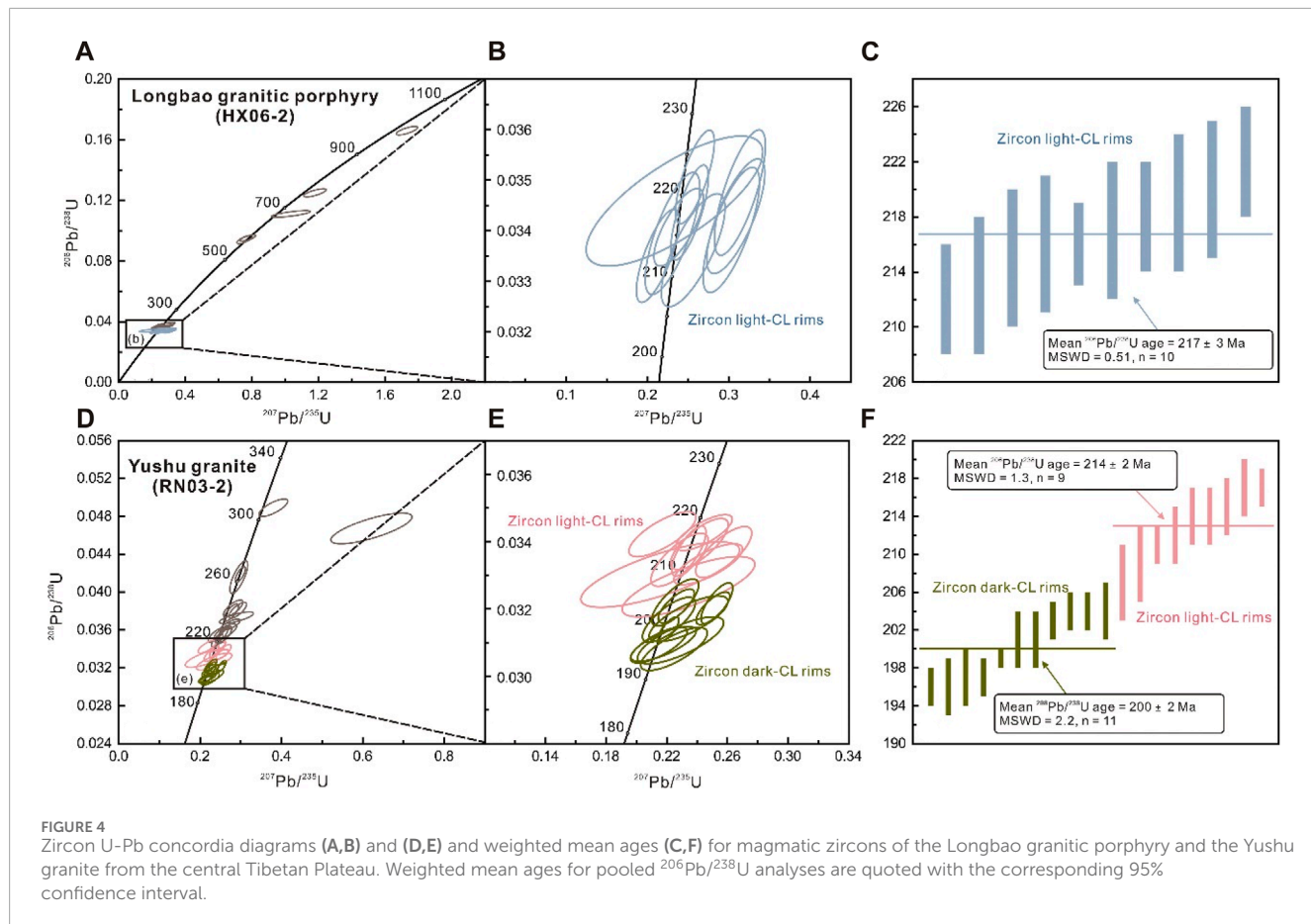
FIGURE 4
Zircon U-Pb concordia diagrams (A,B) and (D,E) and weighted mean ages (C,F) for magmatic zircons of the Longbao granitic porphyry and the Yushu granite from the central Tibetan Plateau. Weighted mean ages for pooled ^{206}Pb/^{238}U analyses are quoted with the corresponding 95% confidence interval.

ratio of 0.710274 ± 0.000009 and a mean ^{146}Nd/^{144}Nd ratio of 0.512118 ± 0.000009, respectively.

4 Results

4.1 Zircon internal texture and U-Pb geochronology

A Longbao granitic porphyry sample (HX06-2) and a Yushu granite sample (RN03-2) were selected for zircon U-Pb isotopic dating; the results are listed in Table 1.

Zircons from the sample HX06-2 were euhedral-subhedral prismatic crystals, and they had lengths of ~50–130 μm, with an aspect ratio of 1:1 to 2:1. Most of them exhibited apparent oscillatory zoning, and some showed resorbed cores on CL images. Ten analyses of the zircon rims yielded younger ^{206}Pb/^{238}U ages of 212–222 Ma. The weighted mean ^{206}Pb/^{238}U age was 217 ± 3 Ma (MSWD = 0.51; Figures 4A–C), which represents the crystallization age of the Longbao granitic porphyry. The other ten spots yielded relatively old ^{206}Pb/^{238}U ages of 225–989 Ma, which can be interpreted as the ages of the inherited zircons.

Zircons from the sample RN03-2 were euhedral to subhedral prismatic crystals with light yellow to brown colors. Their lengths ranged from 40 μm to 150 μm. Unlike the monotonous oscillatory zoning of zircon in the Longbao granitic porphyry, zircons from the Yushu granite showed complex internal structures, as revealed by CL and transmitted light images (Figure 3B). Zircon grains from the Yushu granite could be subdivided into two groups based on zircon internal structure and age. Group 1 zircons showed light-CL rims and oscillatory zonings on CL images, and they were transparent under transmitted light (Figure 3B), which makes them similar to the zircons from the Longbao granitic porphyry. Group 2 zircons exhibited distinct dark-CL rims on CL images, and these zircons were murky brown and generally translucent under transmitted light (Figure 3B). Nine spots on the zircon with light-CL rims yielded ^{206}Pb/^{238}U ages ranging from 207 Ma to 217 Ma, with a weighted mean ^{206}Pb/^{238}U age of 214 ± 2Ma (MSWD = 1.3). In the other group of zircons with dark-CL rims, eleven rim spots yielded ^{206}Pb/^{238}U ages of 196–204 Ma, with a weighted mean ^{206}Pb/^{238}U age of 200 ± 2 Ma (MSWD = 2.2; Figures 4D–F). In addition, fifteen analysis spots on old inherited cores yielded ^{206}Pb/^{238}U ages between 221 and 308 Ma.

4.2 Zircon trace element composition and Ti-in-zircon geothermometer

Trace element concentrations of zircon grains from the Longbao granitic porphyry sample (HX06-2) and the Yushu granite sample (RN03-2) were determined by LA-ICP-MS; the results are tabulated in Table 2. The results of magmatic zircon analysis were plotted to

assess the conditions of zircon growth during the generation of the respective intrusions (Figure 5).

Zircons from the Longbao granitic porphyry exhibited steeply increasing chondrite-normalized REE patterns from La to Lu, and positive Ce and negative Eu anomalies (Figure 5A). The patterns for these zircons indicated low Hf, Y, Th, and U concentrations, with relatively high Ti concentrations and Th/U ratios (Figure 5B and Figure 6), which are similar to those of typical unaltered igneous zircons, as described by Hoskin and Schaltegger (2003).

The two groups of zircons from the Yushu granite exhibited markedly different trace element compositions. Zircons with light-CL rims had low Hf and Y concentrations, with moderate Th and U concentrations and Th/U ratios. Additionally, the chondrite-normalized REE patterns were steep, with positive Ce and negative Eu anomalies (Figure 5C). These could also be comparable to the characteristics of typical unaltered igneous zircons. However, zircons with dark-CL rims showed enrichment in LREE and MREE

and high abundances of Hf, Y, Th, and U, with low Th/U ratios (Figure 6). These features are distinct from those of unaltered magmatic zircon, which could be interpreted as indicative of hydrothermal origin (Hoskin, 2005). Thus, the weighted mean $^{206}Pb/^{238}U$ age of 214 ± 2Ma can be interpreted as the crystallization age of the Yushu granite, while the younger weighted mean $^{206}Pb/^{238}U$ age of 200 ± 2 Ma for the dark rims may reflect the Pb loss caused by the late hydrothermal process. To estimate the crystallization temperature for minerals removed from their original petrologic context, we selected the Ti-in-zircon thermometry method of Ferry and Watson (2007). It is necessary to consider the activity factors of α_{TiO_2} and α_{SiO_2} before the application of Ti-in-zircon thermometry. Recent modeling results for different granite types have shown that SiO_2-rich and peraluminous granites have a narrow α_{TiO_2} range of ~0.5 and relatively consistent α_{SiO_2} values of ~1 (Schiller and Finger, 2019). Because all the samples were characterized by high SiO_2 contents and were slightly to strongly

TABLE 2 Trace elements of zircons for the Longbao granitic porphyry (HX06-2) and the Yushu granite (RN03-2) in the central Tibetan Plateau.

Spot No.	Ti	Y	Nb	La	Ce	Pr	Nd	Sm	Eu	Gd	Tb	Dy	Ho	Er	Tm	Yb	Lu	Hf	Ta	Th	U
HX06-2																					
1	25.4	4,276	17.9	0.2	29	0.6	8.5	16.6	0.7	89.8	32.0	395	143	644	131	1,230	222	27,513	8.1	547	1,031
2	17.0	958	2.3	0.7	16	0.7	3.7	3.2	0.7	14.0	4.9	62	29	146	38	424	95	26,582	1.2	240	563
3	18.1	2,711	4.2	0.0	20	0.1	3.2	8.2	1.8	42.2	17.2	210	87	426	92	918	183	23,756	1.8	209	439
4	17.6	1,558	3.2	0.0	17	0.1	1.4	4.2	1.3	26.1	9.3	121	49	241	54	531	106	24,637	1.5	155	340
5	21.3	1,421	3.1	0.0	15	0.1	1.8	3.4	0.8	19.0	7.6	102	43	225	52	577	124	26,666	1.6	181	471
6	16.2	1,540	2.9	2.3	20	0.7	4.2	3.6	0.9	22.9	8.8	108	48	239	57	596	124	26,936	1.7	253	567
7	19.7	4,095	2.7	0.0	24	0.6	9.6	16.0	3.8	81.8	27.7	348	134	614	130	1,292	255	26,646	1.6	489	719
8	17.6	1,415	2.2	0.0	8	0.0	0.7	3.3	0.4	21.1	7.8	112	43	222	50	543	116	26,117	1.1	143	386
9	28.1	3,830	13.0	0.2	16	0.4	4.2	11.8	0.2	66.1	26.6	336	130	586	119	1,118	201	31,080	7.2	575	1,033
10	21.4	2,902	5.1	0.1	25	0.3	3.9	8.1	2.0	47.8	17.2	220	93	457	98	1,038	214	26,873	1.9	349	676
11	19.1	1903	3.8	1.2	24	1.2	6.2	7.4	1.4	27.6	9.8	137	57	301	70	761	165	27,689	2.8	296	737
12	16.7	1,673	3.3	0.0	17	0.1	1.4	5.5	1.2	29.5	9.9	130	54	264	57	579	114	25,943	1.4	153	335
13	14.2	2,218	5.3	0.0	24	0.1	3.5	6.0	1.3	38.1	12.5	164	66	332	79	841	181	29,099	3.1	612	1,192
14	36.0	1,273	3.5	3.2	45	3.0	16.3	8.7	1.3	23.3	8.1	99	39	192	46	486	99	29,402	1.7	220	437
15	21.8	2,159	3.7	0.1	19	0.1	2.6	5.8	1.3	33.8	12.3	165	70	342	77	801	167	25,464	2.0	198	458
16	23.0	2,107	3.5	0.0	21	0.1	1.7	6.8	1.1	30.3	12.2	161	67	334	74	748	150	25,370	2.2	201	454
17	1,174.6	1955	30.7	1.9	26	1.3	10.3	7.7	1.2	22.4	9.4	140	60	322	84	981	206	33,499	3.4	470	1830
18	15.8	3,530	12.4	0.1	31	0.1	1.9	7.2	0.6	53.2	21.9	289	114	538	117	1,174	222	34,846	7.4	290	921
19	16.0	5,992	5.5	0.3	15	0.3	4.3	12.7	0.6	97.4	39.9	525	193	890	180	1,654	292	35,337	4.8	684	2,254
20	9.9	9,270	109.7	16.2	174	9.8	61.4	45.2	3.0	191.5	70.3	869	322	1,375	263	2,314	379	25,491	23.6	392	578

TABLE 2 (*Continued*) Trace elements of zircons for the Longbao granitic porphyry (HX06-2) and the Yushu granite (RN03-2) in the central Tibetan Plateau.

Spot No.	Ti	Y	Nb	La	Ce	Pr	Nd	Sm	Eu	Gd	Tb	Dy	Ho	Er	Tm	Yb	Lu	Hf	Ta	Th	U
RN03-2																					
1	9.3	4,685	22.9	0.3	13	0.3	4.3	6.5	1.3	56.9	22.7	327	136	716	158	1858	320	32,257	8.1	542	2,379
2	21.7	3,531	16.5	0.4	14	0.4	4.7	9.1	1.6	52.4	18.7	261	103	524	114	1,315	224	27,994	4.6	613	1,289
3	12.7	3,542	15.3	0.2	11	0.1	2.5	6.6	1.3	45.0	17.6	253	99	524	118	1,386	243	30,774	5.3	675	1835
4	6.2	17,520	271.0	4.1	44	1.4	7.3	15.0	1.1	167.3	81.1	1,284	499	2,459	501	5,211	807	44,254	119.7	4,454	33,865
5	9.9	4,709	20.0	0.2	14	0.2	2.3	7.9	1.0	57.9	22.9	347	137	721	154	1760	291	30,593	6.3	459	1834
6	17.1	6,803	46.5	0.6	28	0.4	5.7	13.6	3.1	87.4	36.7	492	195	1,012	220	2,521	419	31,381	13.3	2019	5,029
7	15.5	4,149	28.2	2.4	43	1.5	8.9	14.1	2.0	71.4	26.4	336	125	612	132	1,469	245	27,812	6.7	1,248	2,386
8	14.6	3,751	14.4	0.0	11	0.1	3.0	5.8	1.0	45.5	18.3	275	111	565	123	1,440	244	25,986	4.4	420	1,243
9	23.0	4,003	30.3	1.0	20	0.7	6.1	10.5	1.4	58.5	21.7	290	116	600	133	1,532	265	28,527	5.4	586	1,499
10	9.4	4,846	9.4	0.3	24	0.6	7.5	14.6	2.5	85.2	28.2	379	139	700	148	1,683	287	29,348	3.4	897	1831
11	10.6	13,358	222.0	15.0	74	5.9	31.7	24.0	5.5	158.7	66.8	998	382	1907	388	4,147	649	47,252	250.5	2,898	24,917
12	6.5	7,736	60.9	0.0	12	0.1	1.8	6.8	1.0	73.1	34.1	537	222	1,163	247	2,745	439	35,015	25.1	736	5,294
13	11.0	4,232	6.8	0.2	14	0.6	9.2	15.6	3.3	82.1	26.8	328	124	610	127	1,474	242	26,691	2.3	684	1,235
14	4.5	11,625	156.6	0.5	16	0.3	2.1	9.0	1.8	108.2	52.4	855	342	1738	363	3,969	621	36,811	52.6	1842	15,565
15	10.7	10,168	117.7	0.1	26	0.2	3.1	13.1	1.8	125.8	49.2	744	293	1,468	307	3,350	542	30,143	32.4	2,848	9,708
16	11.1	6,473	26.3	0.0	19	0.1	3.8	11.5	2.0	86.3	33.8	491	189	963	203	2,258	372	28,852	7.7	1,139	2,682
17	60.2	21,665	413.8	6.2	58	3.8	18.9	23.5	1.9	195.2	98.0	1,534	613	3,132	639	6,927	1,081	40,987	119.3	3,185	33,501
18	22.9	4,423	25.5	1.8	23	1.1	9.3	10.1	1.9	65.4	24.6	330	127	676	142	1,657	287	25,624	5.4	649	1815
19	25.8	7,697	176.9	17.3	126	10.6	56.6	47.7	4.1	168.3	55.0	669	228	1,069	213	2,294	361	34,995	34.4	2,147	11,179
20	13.9	4,251	18.4	0.2	15	0.2	3.5	7.3	1.0	51.0	20.4	296	121	640	144	1701	295	28,377	6.2	565	1817
21	13.8	4,221	20.3	0.0	15	0.2	3.0	9.0	1.5	56.0	20.5	297	122	638	140	1,644	282	27,120	6.9	719	1845
22	20.8	3,301	82.1	17.8	538	12.7	77.7	62.0	6.8	146.4	33.8	344	103	452	92	1,059	166	29,610	13.4	701	1,456
23	12.0	5,699	65.7	1.7	25	1.4	6.2	12.3	2.5	91.3	32.2	441	168	856	181	1971	321	31,805	16.2	2067	6,032
24	4.6	20,880	315.1	5.9	56	3.1	19.1	24.1	2.8	214.1	94.4	1,491	593	3,014	605	6,305	983	39,659	105.9	6,072	29,337
25	12.7	5,416	9.5	0.1	18	1.2	14.3	26.3	5.0	105.3	34.0	418	156	775	163	1989	340	23,946	3.7	1,290	2,107
26	17.6	14,631	201.7	54.2	276	27.1	145.7	85.4	30.9	300.5	101.1	1,219	423	1988	375	3,926	597	32,707	59.3	7,143	22,880
27	35.8	14,180	163.5	61.7	462	38.9	229.6	134.4	20.9	387.6	108.7	1,250	400	1802	343	3,663	555	29,614	40.9	2,549	12,166
28	54.2	12,674	287.2	24.2	151	17.9	100.7	80.4	8.1	282.9	99.4	1,154	433	1888	398	3,660	648	37,849	64.8	2,524	17,790
29	9.8	2,825	35.9	2.0	9	0.4	2.1	2.8	7.9	34.0	16.4	216	96	454	106	1,071	211	35,943	20.5	465	3,032
30	9.0	14,040	182.2	23.4	130	10.7	50.9	41.1	29.5	184.4	81.0	1,125	471	2,184	477	4,473	803	54,348	99.4	1,455	17,739
31	9.0	17,933	252.6	1.0	24	0.4	5.0	17.8	1.5	204.6	102.3	1,447	590	2,717	579	5,377	948	38,322	107.8	3,603	21,823

(Continued on the following page)

TABLE 2 (*Continued*) Trace elements of zircons for the Longbao granitic porphyry (HX06-2) and the Yushu granite (RN03-2) in the central Tibetan Plateau.

Spot No.	Ti	Y	Nb	La	Ce	Pr	Nd	Sm	Eu	Gd	Tb	Dy	Ho	Er	Tm	Yb	Lu	Hf	Ta	Th	U
32	55.2	16,177	246.8	43.7	307	33.2	178.1	119.4	15.5	342.7	111.7	1,329	529	2,400	511	4,814	870	39,027	78.6	1847	12,835
33	14.3	15,362	303.9	37.7	245	22.1	109.3	66.9	11.0	256.9	99.4	1,303	509	2,307	496	4,646	820	54,490	294.7	2,562	29,241
34	245.4	13,236	258.4	99.6	523	59.2	325.6	152.7	113.7	376.9	111.5	1,249	424	1788	371	3,348	573	55,210	364.7	3,077	26,945
35	4.2	16,865	251.9	0.1	33	0.1	2.8	20.4	2.3	235.2	110.4	1,444	587	2,536	522	4,667	814	33,596	86.9	8,600	30,806

peraluminous, activity factors of $\alpha_{SiO_2} = 1$ and $\alpha_{TiO_2} = 0.5$ were used to estimate the Ti-in-zircon temperature. Calculations for zircons with light-CL rims from the Yushu granite showed a relatively high Ti-in-zircon temperature (771–913°C, average 842°C), and zircons from the Longbao granitic porphyry also exhibited a markedly high Ti-in-zircon temperature (873–972°C, average 904°C).

4.3 Whole-rock major and trace elements

The results of whole-rock geochemical analyses and the relevant parameters calculated are listed in Table 3. LOI values were relatively low (0.25–0.59 wt%), and neither the mobile nor the immobile elements exhibited any correlation with LOI (Supplementary Figure S1), suggesting insignificant alteration.

Samples of the Longbao granitic porphyry were characterized by high SiO_2 (75.98–76.78 wt%) and K_2O (4.40–5.43 wt%) content, but low CaO (0.99–1.15 wt%), TiO_2 (0.10–0.16 wt%), FeO^T (0.76–1.03 wt%), MgO (0.25–0.38 wt%), and P_2O_5 (0.02–0.04 wt%) content (Table 3). These were plotted in the field of high-K calc-alkaline and magnesian series in classification diagrams (Figures 7B, C). In addition, those samples were slightly peraluminous, with A/CNK ratios ranging from 1.02 to 1.06 (Figure 7D). Those samples had higher total rare earth element concentrations (ΣREE = 103.8–125.2 ppm) than the Yushu granite samples. In chondrite-normalized REE diagrams, the samples were characterized by enrichment of LREE relative to HREE [(La/Yb)$_N$ = 12.50–18.68], a flat HREE pattern [(Gd/Yb)$_N$ = 0.92–1.32], and variable negative Eu anomalies (δEu = 0.43–0.76; Figure 8A). On a primitive mantle-normalized spider diagram, all the samples showed obvious depletion of Ba, Nb, Sr, P, and Ti, but enrichment of Th, U, and Rb (Figure 8B).

Samples of the Yushu granite showed high SiO_2 (75.31–75.99 wt%) and K_2O (3.69–4.43 wt%) content, but low CaO (0.95–1.65 wt%), TiO_2 (0.03–0.08 wt%), FeO^T (0.69–1.05 wt%), MgO (0.15–0.30 wt%), and P_2O_5 (0.01–0.02 wt%) content (Table 3). They were plotted in the field of high-K calc-alkaline and magnesian series according to classification diagrams (Figures 7B, C). In addition, these samples were slightly to strongly peraluminous, with A/CNK ratios ranging from 1.05 to 1.13 (Figure 7D). The samples were characterized by moderate concentrations of total rare earth elements (ΣREE = 93.2–98.6 ppm) and negative Eu anomalies (δEu = 0.25–0.55). On a chondrite-normalized diagram, all the samples exhibited flat REE patterns [(La/Yb)$_N$ = 1.13–3.23 (Gd/Yb)$_N$ =

0.77–1.13] (Figure 8C). On a primitive mantle-normalized spider diagram, all the samples were enriched in large-ion lithophile elements (LILEs), such as Rb, Th, and U, and exhibited depleted high field strength elements (HFSEs), such as Sr, Ba, P, and Ti (Figure 8D).

4.4 Whole-rock Sr-Nd isotopes

Whole-rock Sr-Nd isotopic compositions of the granites studied are listed in Table 4; initial Sr and Nd isotopic ratios (I$_{Sr}$) and $\varepsilon_{Nd}(t)$ values were calculated based on the timing of 215 Ma. The sample from the Longbao granitic porphyry showed an initial $^{87}Sr/^{86}Sr$ ratio of 0.7120 and $\varepsilon_{Nd}(t)$ value of −7.58, with the corresponding depleted-mantle model age (T$_{2DM}$) of 1.61 Ga. The samples from the Yushu granite were characterized by relatively high $(^{87}Sr/^{86}Sr)_i$ ratios, in the range of 0.7121–0.7136, and low $\varepsilon_{Nd}(t)$ values of −8.58 to −7.97, with a T$_{2DM}$ age of 1.64–1.69 Ga.

5 Discussion

5.1 Genetic types

In a seminal paper, Chappell and White (1974) classified the granites of the Lachlan Fold Belt (LFB) in south-eastern Australia into two end-members: I- and S-type granites. This classification has become well-established in most granites that have diverse sources and has developed into the current I-S-M-A classification of granitoids. M-type granites, which are distinguished by relatively low K_2O (<1.9 wt%) and Rb (<48 ppm) values, are derived directly from the melting of subducted oceanic crust or overlying mantle (Saito et al., 2004). A-type (alkaline, anhydrous, and anorogenic) granites exhibit notably high values of 10,000×Ga/Al (>2.6) and Zr+Nb+Ce+Y (>350 ppm) (Whalen et al., 1987), which are associated with ferroan granitic melts (Frost et al., 2001). The samples of Yushu granite and Longbao granitic porphyry were plotted in the field of high-K calc-alkalic and magnesian series (Figure 7) and exhibited low values of 10,000×Ga/Al; these characteristics do not correspond with those of the A- and M-type granites. The granites studied consisted primarily of plagioclase, alkali-feldspar, and quartz, with minor biotite and an absence of amphibole (Figure 2), tending to be close to haplogranite (near minimum-temperature melt; King et al.,

TABLE 3 Bulk-rock major and trace elements data for the Yushu granite and the Longbao granitic porphyry, central Tibetan Plateau.

Sample No.	LB08-2	HX06-2	HX06-1	HX06-3	HX06-5	RN01-1	RN02-2	RN03-1	RN03-2	RN04-1	RN05-1
SiO_2	76.27	75.98	76	76.78	76.52	75.9	75.96	75.99	75.71	75.31	75.78
TiO_2	0.13	0.16	0.12	0.12	0.1	0.07	0.04	0.06	0.06	0.08	0.03
Al_2O_3	12.81	12.68	12.72	12.7	12.54	13.38	13.46	13.4	13.31	13.64	13.66
Fe_2O_3	0.05	0.35	0.22	0.2	0.15	0.37	0.19	0.11	0.16	0.28	0.24
FeO	0.78	0.72	0.6	0.58	0.63	0.72	0.63	0.68	0.82	0.78	0.47
FeOt	0.82	1.03	0.80	0.76	0.76	1.05	0.80	0.78	0.96	1.03	0.69
MnO	0.01	0.02	0.01	0.01	0.01	0.07	0.09	0.05	0.07	0.07	0.1
MgO	0.28	0.38	0.28	0.25	0.28	0.3	0.15	0.21	0.27	0.27	0.15
CaO	0.99	1.15	0.95	1.06	1.03	1.58	1	1.38	1.645	1.61	0.96
Na_2O	3.31	3.21	3.34	3.2	2.73	3.32	3.52	3.22	3.26	3.31	3.4
K_2O	4.7	4.66	4.85	4.4	5.43	3.69	4.17	4.16	3.95	3.73	4.43
P_2O_5	0.04	0.04	0.03	0.04	0.02	0.02	0.01	0.02	0.02	0.02	0.01
CO_2	0.06	0.05	0.01	0.02	0.05	0.13	0.05	0.13	0.16	0.13	0.02
H_2O^+	0.4	0.43	0.49	0.47	0.37	0.31	0.48	0.35	0.37	0.5	0.53
LOI	0.38	0.59	0.38	0.37	0.25	0.38	0.44	0.44	0.56	0.58	0.38
Total	99.83	99.83	99.62	99.83	99.86	99.86	99.75	99.76	99.81	99.73	99.78
Li	6.2	5.8	5.1	6.9	5.3	85.5	72.4	47.7	71.2	85.9	52.3
Be	2.34	2.31	2.31	2.50	2.00	3.28	3.40	3.14	3.01	3.84	3.26
Sc	2.86	2.44	2.61	3.26	3.11	4.30	4.71	3.87	3.96	4.12	4.48
V	7.36	6.43	5.06	5.73	5.89	3.39	2.33	2.61	2.80	2.89	1.36
Cr	19.12	3.85	3.76	3.35	3.35	1.35	0.69	0.94	1.63	2.21	1.02
Co	85	69	85	107	90	153	128	149	118	134	134
Ni	4.44	3.04	2.67	3.38	2.45	2.23	2.69	2.25	2.71	2.15	2.81
Cu	39.46	22.85	48.39	41.46	2.82	3.90	1.15	1.99	2.40	2.20	0.93
Zn	8.9	10.4	7.2	7.4	11.1	32.4	29.6	28.3	28.6	35.4	19.6
Ga	11.9	12.4	11.9	12.6	12.6	15.5	15.9	14.9	14.6	15.5	15.3
Rb	158	172	161	154	168	188	206	175	167	188	223
Sr	75	82	68	76	51	90	64	86	94	103	46
Y	12.5	12.1	13.4	14.8	12.2	31.5	44.5	39.3	30.0	26.2	41.9
Zr	80	81	77	79	91	51	49	56	70	61	55
Nb	8.2	8.2	8.1	9.4	9.2	15.9	17.2	12.2	12.7	14.8	15.8

(Continued on the following page)

TABLE 3 (*Continued*) Bulk-rock major and trace elements data for the Yushu granite and the Longbao granitic porphyry, central Tibetan Plateau.

Sample No.	LB08-2	HX06-2	HX06-1	HX06-3	HX06-5	RN01-1	RN02-2	RN03-1	RN03-2	RN04-1	RN05-1
Mo	0.23	0.08	0.08	0.09	0.06	0.08	0.09	0.11	0.08	0.07	0.07
Sn	1.25	0.89	0.50	0.32	1.63	11.23	7.10	5.13	7.44	10.68	7.11
Cs	3.69	5.30	3.08	2.30	3.71	8.70	5.78	4.92	7.04	9.71	7.13
Ba	446	511	413	470	383	299	213	312	345	375	172
La	25.3	26.0	29.2	30.5	29.7	10.7	6.8	8.0	11.0	12.2	6.6
Ce	42.2	42.2	48.6	51.1	51.2	22.2	14.4	17.6	23.0	24.6	13.9
Pr	3.65	3.64	4.19	4.51	4.56	2.50	1.66	1.97	2.59	2.71	1.61
Nd	11.08	11.28	12.54	13.66	13.68	9.83	6.65	7.89	9.87	10.41	6.48
Sm	1.88	1.80	2.02	2.24	2.27	3.24	2.70	2.80	2.87	2.73	2.50
Eu	0.43	0.41	0.37	0.44	0.29	0.47	0.35	0.45	0.52	0.55	0.26
Gd	1.67	1.44	1.70	1.88	1.74	3.78	3.87	4.16	3.63	3.42	3.98
Tb	0.29	0.27	0.31	0.33	0.28	0.75	0.87	0.85	0.65	0.60	0.85
Dy	1.87	1.64	1.89	2.14	1.74	4.65	6.19	5.61	4.42	3.88	5.85
Ho	0.38	0.34	0.37	0.43	0.34	0.94	1.31	1.18	0.87	0.78	1.18
Er	1.17	1.09	1.20	1.34	1.05	2.75	4.04	3.38	2.76	2.37	3.53
Tm	0.20	0.16	0.20	0.21	0.16	0.42	0.62	0.47	0.43	0.38	0.52
Yb	1.37	1.26	1.41	1.49	1.07	2.80	4.07	2.98	2.81	2.55	3.56
Lu	0.20	0.19	0.21	0.21	0.17	0.40	0.58	0.43	0.42	0.37	0.50
Hf	2.86	2.79	2.76	2.76	3.43	2.49	2.86	2.70	2.99	2.66	3.21
Ta	1.76	1.62	1.67	1.77	1.27	2.65	2.75	1.86	2.50	2.58	3.97
Tl	0.50	0.57	0.49	0.37	0.66	0.93	1.05	0.84	0.82	0.95	1.06
Pb	23.7	30.3	23.6	17.8	30.4	36.8	43.2	40.4	36.9	36.4	46.1
Th	18.9	20.1	19.2	18.5	21.4	8.3	6.9	8.0	8.1	8.1	8.3
U	4.24	3.71	3.51	3.88	3.79	2.43	2.48	3.33	2.59	2.72	3.23
ΣREE	104.2	103.8	117.5	125.2	120.5	97.0	98.6	97.1	95.9	93.7	93.2
Eu/Eu∗	0.73	0.76	0.60	0.64	0.43	0.41	0.33	0.40	0.49	0.55	0.25
(La/Yb)$_N$	12.50	13.90	14.03	13.84	18.68	2.58	1.13	1.82	2.65	3.23	1.25

Notes: Eu/Eu∗ = (Eu)$_N$/[(Sm)$_N$×(Gd)$_N$]$^{1/2}$.

1997). Additionally, it is very difficult to discriminate them as I-type or S-type, because both high-silica I- and S-type granites usually have analogous geochemical compositions and mineral assemblages (Wu et al., 2017).

5.2 Magma source and crustal melting

It is widely accepted that Sr-Nd isotopes can trace the magma sources of highly evolved granites, because it is difficult for magma

TABLE 4 Bulk-rock Sr-Nd isotopic compositions of the typical samples in the central Tibetan Plateau.

Sample No.	Rb (ppm)	Sr (ppm)	$^{87}Rb/^{86}Sr$	$^{87}Sr/^{86}Sr$	Sm (ppm)	Nd (ppm)	$^{147}Sm/^{144}Nd$	$^{143}Nd/^{144}Nd$	t (Ma)	Isr	$\varepsilon Nd(t)$	T_{2DM} (Ga)
Yushu granite												
12RN01-1	188	90	6.0431	0.73056	3.2	9.8	0.1994	0.51223	215	0.7121	−7.97	1.64
12RN02-2	206	64	9.2704	0.74096	2.7	6.6	0.2456	0.51227	215	0.7126	−8.58	1.69
Longbao granitic porphyry												
11LB08-2	158	75	6.1464	0.73078	1.9	11.1	0.1024	0.51212	215	0.7120	−7.58	1.61

Notes: $\varepsilon_{Nd}(t) = [(^{143}Nd/^{144}Nd)_{S}(t)/(^{143}Nd/^{144}Nd)_{CHUR}(t) - 1] \times 10,000$.

$T_{2DM} = (1/\lambda) \times \ln\{1 + [(^{143}Nd/^{144}Nd)_{S} - ((^{147}Sm/^{144}Nd)_{S} - ((^{147}Sm/^{144}Nd)_{S} - (^{147}Sm/^{144}Nd)_{C}) \times (e^{\lambda t} - 1))/((^{147}Sm/^{144}Nd)_{C} - (^{147}Sm/^{144}Nd)_{DM})]\}$.

$(^{143}Nd/^{144}Nd)_{DM}$ 0.513151; $(^{147}Sm/^{144}Nd)_{DM}$ 0.2136; $(^{143}Nd/^{144}Nd)_{CHUR}$ 0.512638; $(^{147}Sm/^{144}Nd)_{CHUR}$ 0.1967; $(^{147}Sm/^{144}Nd)_{C} = 0.118$.

$\lambda = 6.54 \times 10^{-12} yr^{-1}$; $t = 215Ma$; s = sample.
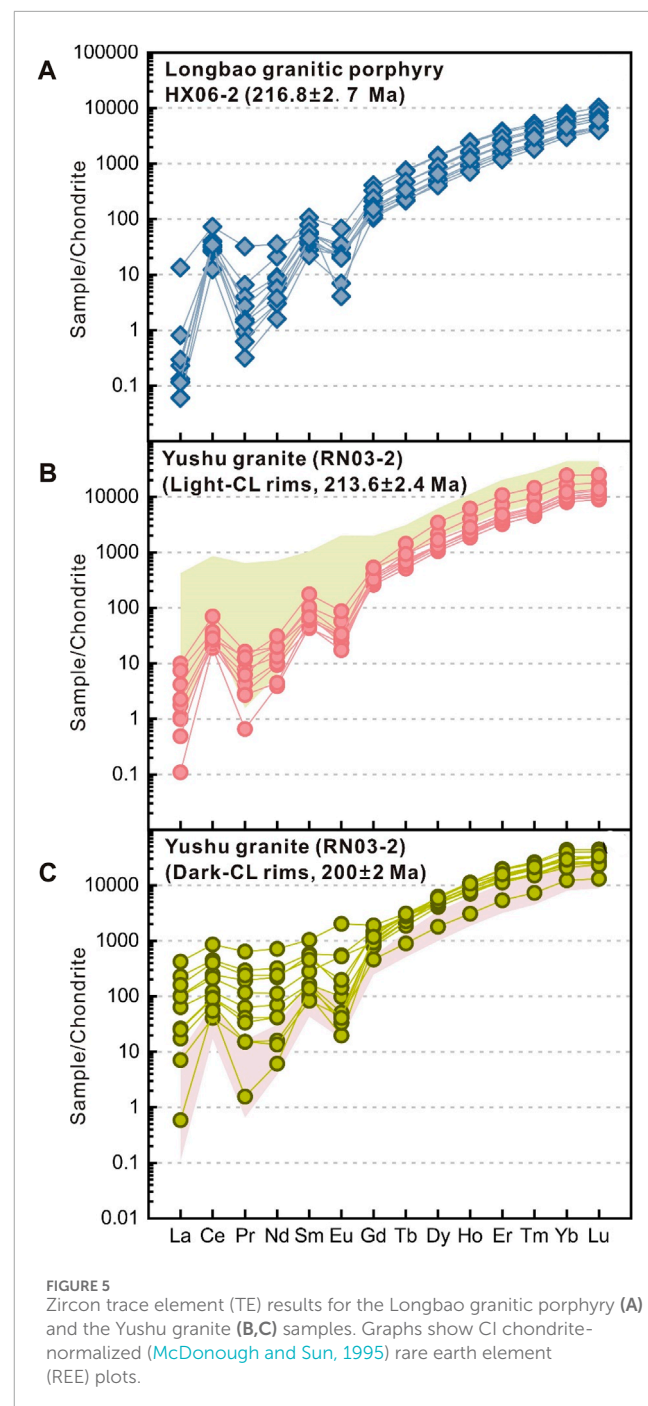
FIGURE 5
Zircon trace element (TE) results for the Longbao granitic porphyry **(A)** and the Yushu granite **(B,C)** samples. Graphs show CI chondrite-normalized (McDonough and Sun, 1995) rare earth element (REE) plots.

differentiation to affect $\varepsilon_{Nd}(t)$ values and Sm/Nd ratios (DePaolo, 1988). Samples from the Longbao granitic porphyry and the Yushu granite exhibited relatively high initial $^{87}Sr/^{86}Sr$ isotope ratios (0.7120–0.7136) and negative $\varepsilon_{Nd}(t)$ values (−8.58 to −7.58), suggesting a large contribution from crustal components.

Two potential candidates involving the widespread Triassic turbidites and the Precambrian basement rocks have been proposed for the crustal sources of Triassic intermediate to acid rocks in the central Tibetan Plateau (Liu et al., 2021). Previous studies have demonstrated that the granites derived from melting of the
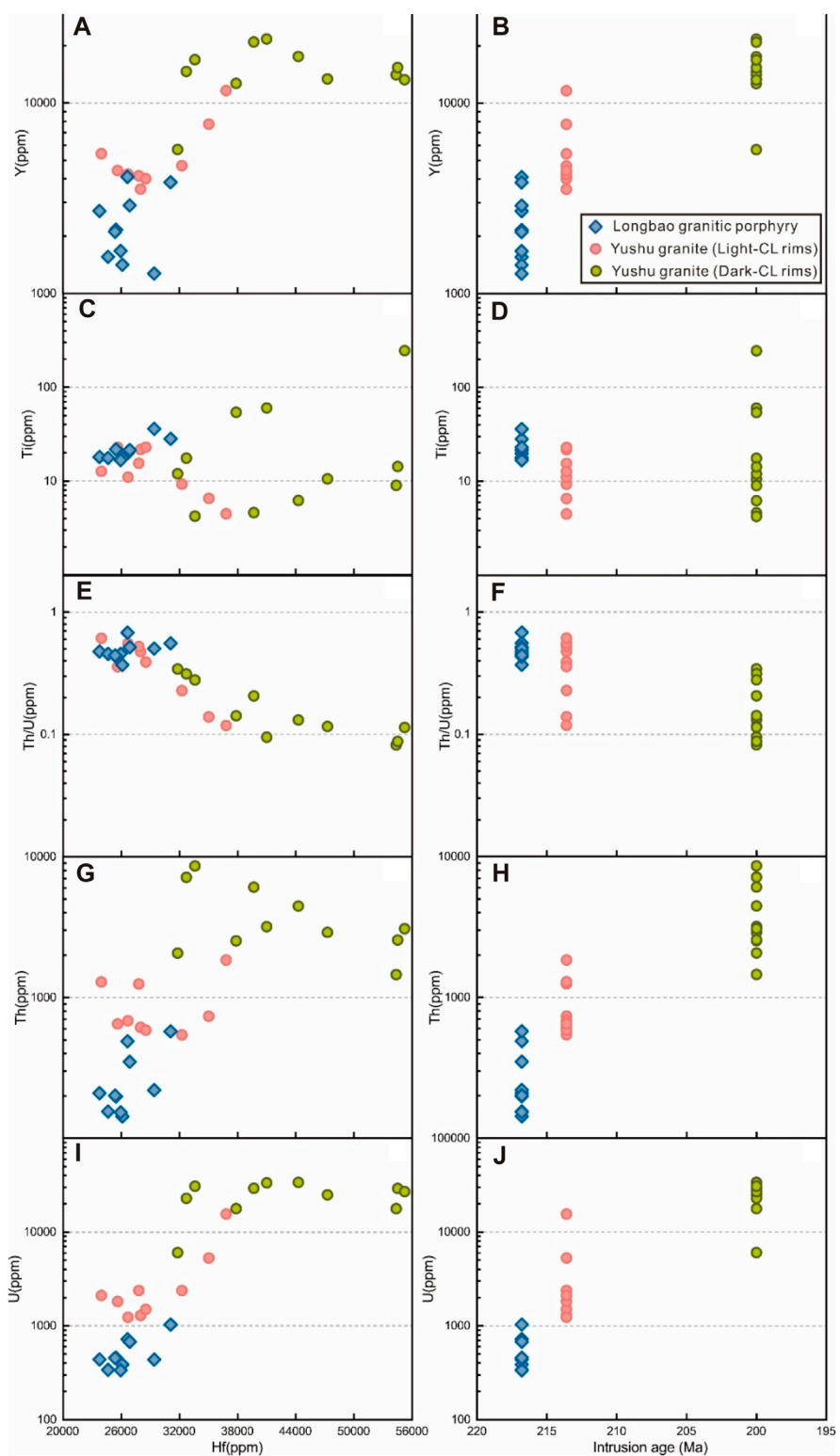
FIGURE 6
Zircon trace element concentrations and ratios plotted against Hf concentration (left column) and age (right column) for the Longbao granitic porphyry and the Yushu granite samples.
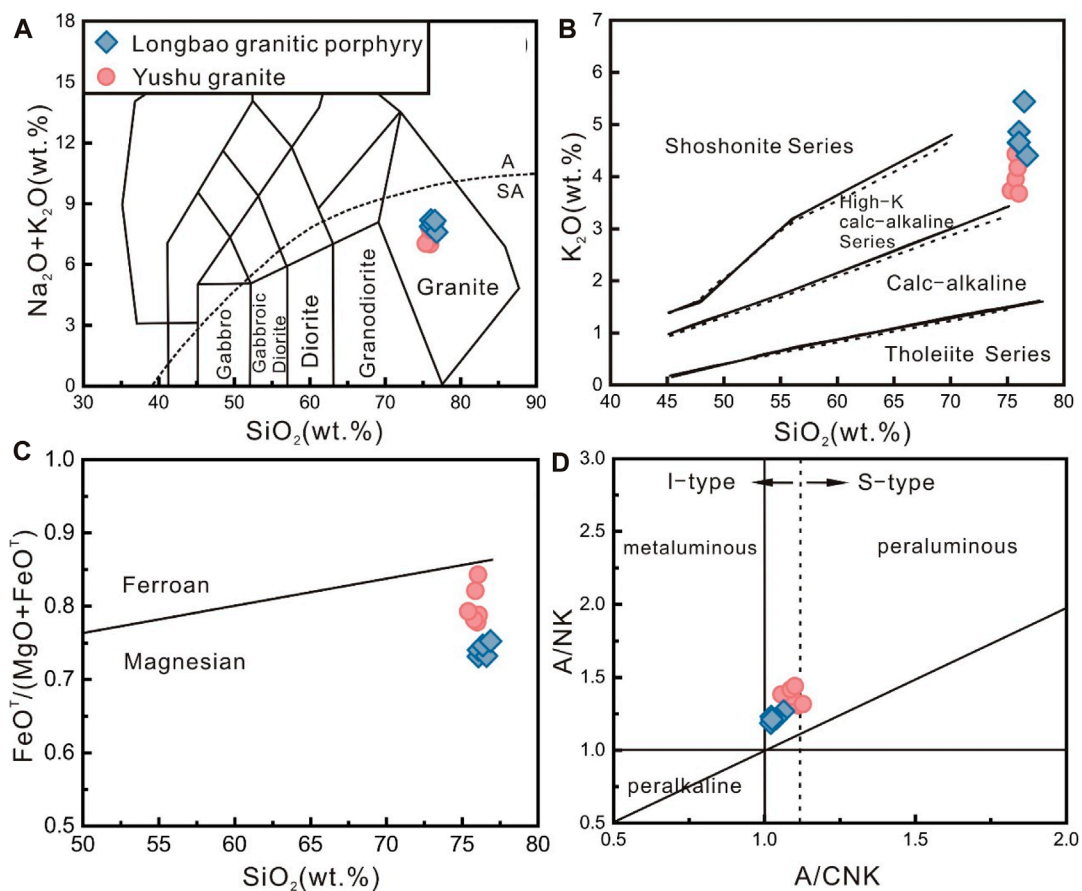
FIGURE 7
Classification diagrams for the granites studied. **(A)** (Na₂O+ K₂O) vs SiO₂ diagram (Middlemost, 1994); alkaline field **(A)** and sub-alkaline field (SA) after Irvine and Baragar (1971). **(B)** K₂O vs SiO₂ diagram (Peccerillo and Taylor, 1976). **(C)** FeO^T/(FeO^T + MgO) vs SiO₂ diagram (Frost et al., 2001). **(D)** A/NK vs A/CNK diagram (Maniar and Piccoli, 1989).

Precambrian basement rocks had higher initial $^{87}Sr/^{86}Sr$ isotope ratios (0.7240–0.7390) and noticeably more negative ε_{Nd}(t) values (−13.26 to −11.13; Tao et al., 2014; Liu et al., 2023), which are distinct from those of the high-silica granites studied here. The Sr-Nd isotopic compositions of the two suites of high-silica granites overlapped with those of the Triassic turbidites in the HBSG terrane (Figure 9), further indicating that the widespread turbidites might be a good candidate for the crustal sources.

High-silica granites are usually considered to originate from pure crustal anatexis, and are usually linked with the process of crustal evolution (Clemens and Stevens, 2012). It is widely accepted that the continental crustal material is not water-enriched, and that the dehydration–melting reaction is the controlling factor in generating the crustal magma (Weinberg and Hasalová, 2015; Wu et al., 2020). Partial melting under vapor-absent and/or vapor-present conditions could produce different residual mineral phases and could cause various distributions of trace elements in the melts (Harris and Inger, 1992). Under vapor-absent conditions, the initial melt would have lower Ca, Sr, and Ba content and higher Rb/Sr ratios compared to vapor-present conditions, because more micas (enrichment of Rb than Sr) and less plagioclase (enrichment of Sr than Rb) are consumed (Harris and Inger, 1992;

Gao et al., 2017). Although fractional crystallization of plagioclase could also result in low CaO and Sr content and a high Rb/Sr ratio, this was not the case for the high-silica granites examined. All the samples from the Longbao granitic porphyry had δEu values above 0.4, and this was also the case for most samples from the Yushu granite. These features indicate a relatively low to moderate degree of plagioclase fractionation (Gao et al., 2017; Zeng and Gao, 2017). Furthermore, fractional crystallization might be not the main factor controlling the generation of high-silica magma, because felsic melts usually have particularly high viscosity (Glazner, 2014). Thus, the low CaO and Sr content and the high Rb/Sr ratio might be more likely to have originated from the composition of the magma source, supporting the dehydration melting reaction (Figure 10). In addition, the proportions of An, Ab, and Or could represent the differences between vapor-absent and vapor-present conditions (Weinberg and Hasalová, 2015). On FeO-Na₂O/K₂O and An-Ab-Or diagrams based on experimental petrological data, the granites studied exhibited trends following the dehydration melting of Bt-Ms schists reported by Patiño Douce and Harris (1998) (Supplementary Figures S1A,B. Moreover, experimental studies have shown that melts derived from Ms-bearing and/or Bt-bearing sources exhibit higher K₂O/Na₂O
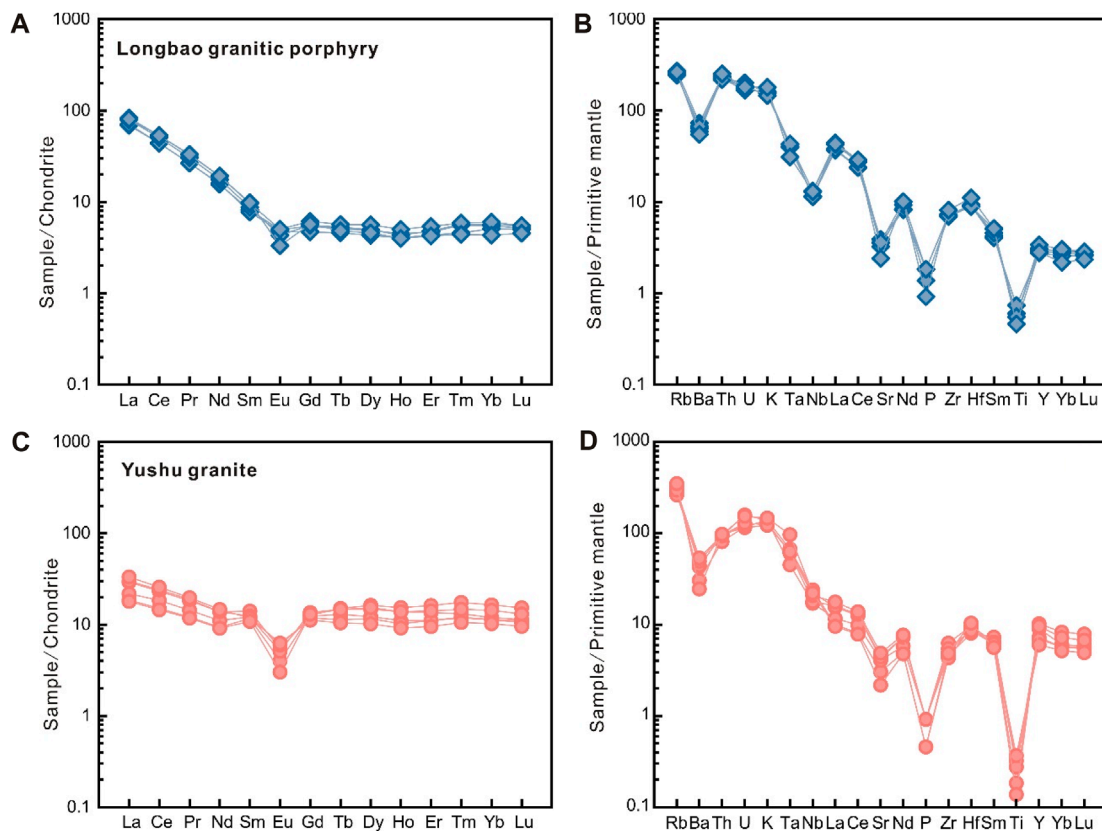
FIGURE 8
Chondrite–normalized REE patterns (A,C) and primitive mantle–normalized spider diagrams (B,D) for the granites studied. Normalizing values of chondrite and primitive mantle are from Taylor and McLennan (1985) and Sun and McDonough (1989), respectively.
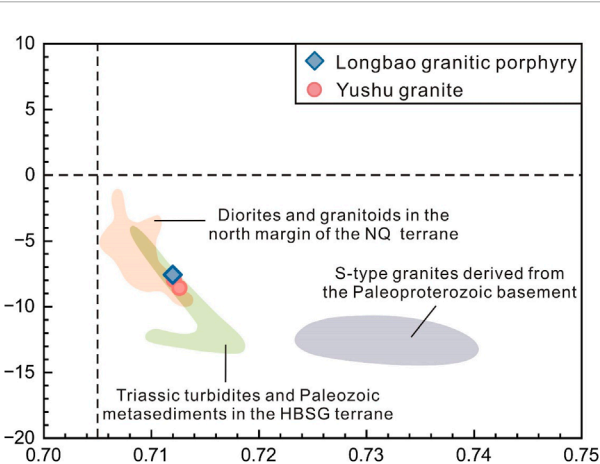
FIGURE 9
Plot of $\varepsilon_{Nd}(t)$ vs $(^{87}Sr/^{86}Sr)_i$ for the granites studied. Data sources: Triassic turbidites and Paleozoic metasediments in the HBSG terrane are from de Sigoyer et al. (2014), She et al. (2006), Zhang et al. (2012), and Zhao et al. (2022); Late Triassic S-type granitoids that were derived from the Paleoproterozoic basement rocks in the NQ terrane are from Liu et al. (2023) and Tao et al. (2014).

ratios (>1.0) than melts derived from Amp-bearing sources (<1.0) (Gao et al., 2016). Samples from the Longbao granitic porphyry and the Yushu granite had relatively high ratios of K_2O/Na_2O (>1.0),

suggesting that they might originate from Bt- and/or Ms-bearing sources. The variation in Rb/Sr, Sr, and Ba further supports the melting of a Ms-bearing crustal source (Figure 10).

5.3 Geodynamic relationship with the paleo-tethyan ocean

The Triassic tectonic evolution of the NQ terrane and adjacent HBSG terrane remains hotly debated, and two conflicting models, the "collision-related model" and the "subduction-related model," have been employed to interpret the generation of Triassic magmatism in the central Tibetan Plateau (Zhang et al., 2007; Yuan et al., 2010; Liu et al., 2021).

The "collision-related model" proposes that the Palaeo-Tethyan ocean closed during Middle Triassic times, and the subsequent crustal thickening and lithospheric delamination triggered the Middle to Late Triassic magmatism (Zhang et al., 2007; Yuan et al., 2010). However, it can be argued based on the identification of a Middle to Upper Triassic submarine fan in the HBSG terrane (Ding et al., 2013) that the ocean could not have closed until Late Triassic times. The zircon U-Pb ages of MORB-type mafic rocks from the ophiolites in the Garzê-Litang suture zone are 239–232 Ma, implying that the Palaeo-Tethyan ocean still existed during Middle Triassic times (Liu et al.,
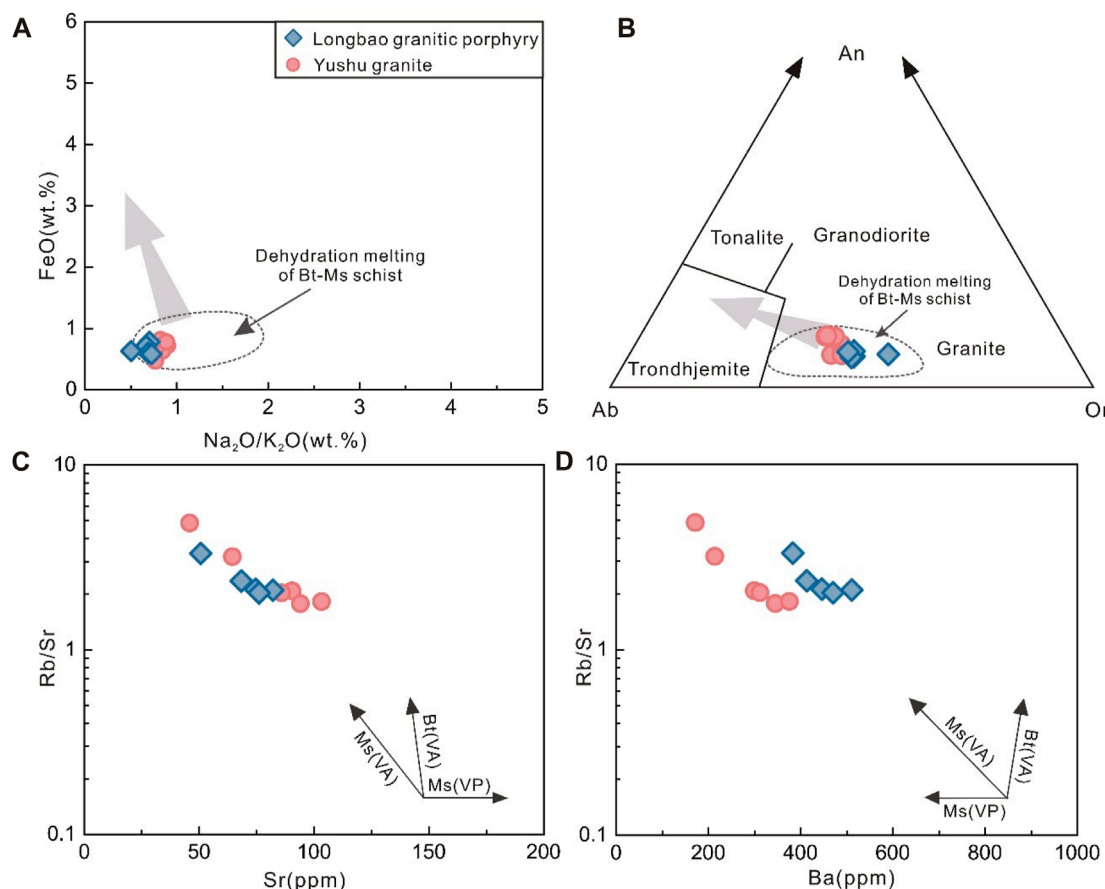
FIGURE 10
(A) FeO vs Na_2O/K_2O diagram. **(B)** An-Ab-Or normative triangle diagram. The circle of dehydration melting of Bt-Ms schist is from Patiño Douce and Harris (1998). Gray arrows point in the direction of melt composition change from dehydration melting to water-present melting. **(C)** Rb/Sr vs Sr diagram. **(D)** Rb/Sr vs Ba diagram (Inger and Harris, 1993). VP, vapor-present; VA, vapor-absent; Bt, biotite; Ms, muscovite.

2016a). A series of adakites-high-Mg andesites-Nb-rich basalts with ages of ~229 Ma have been identified in the Tuotuohe area, indicating that the oceanic subduction might have begun at ~229 Ma (Wang et al., 2008). With the southward subduction of the Garzê-Litang ocean, arc volcanic rocks with ages of 230–209 Ma (Yang et al., 2012; Zhao et al., 2014; Liu et al., 2016b; Liu et al., 2020; Liu et al., 2022) developed along the northwest–southeast direction (Figure 1). In addition, new paleolatitude data indicate that the final closure of the Palaeo-Tethyan ocean might have occurred at 213–204 Ma (Song et al., 2015). The timing of the ductile deformation of the collision stage may be recorded in metamorphic minerals (e.g., biotite and muscovite), and ^{40}Ar-^{39}Ar analyses of these have yielded ages of 201–193 Ma (Yang et al., 2012; Zhang et al., 2013). Therefore, the high-silica granites (217–214 Ma) in this study were probably formed in a subduction environment.

Moreover, samples from the Longbao granitic porphyry and the Yushu granite exhibited high apparent Ti-in-zircon temperatures, indicating a significant thermal anomaly at the deep crustal levels. Wang et al. (2008) proposed that the oceanic lithosphere might have subducted to depths of ~85 km at ~229 Ma. With this deepening of the depths of subduction, intensive eclogite-facies

metamorphism increased the density of the subducted oceanic lithosphere, subsequently leading to slab roll-back (Liu et al., 2021). Slab roll-back in turn would induce upwelling of the asthenosphere and provide sufficient heat for crustal melting. If this was the case, partial melting of a Ms-bearing crustal source would have induced the Late Triassic magmatism in the North Qiangtang terrane, including the Longbao granitic porphyry and the Yushu granite.

6 Conclusion

(1) Two suites of Late Triassic high-silica granites have been identified in the North Qiangtang terrane in the central Tibetan Plateau. The results of zircon U-Pb dating indicate that the crystallization ages of those high-silica granites are 217–214 Ma.

(2) The Late Triassic high-silica granites were mainly produced by dehydration melting of a Ms-bearing source, and the Triassic turbidites might be a good candidate for the magma source.

(3) The high-silica granites (217–214 Ma) examined in this study were probably formed in a subduction environment, and partial melting of Triassic turbidites induced by slab roll-back might be the key factor controlling the origin of Late Triassic magmatism in the North Qiangtang terrane.

Data availability statement

The original contributions presented in the study are included in the article/Supplementary Material, further inquiries can be directed to the corresponding author.

Author contributions

CJ: Writing–original draft. BL: Writing–review and editing. YC: Investigation, Writing–review and editing. ZW: Writing–review and editing. CC: Writing–review and editing.

Funding

Acknowledgments

Conflict of interest

The authors declare that the research was conducted in the absence of any commercial or financial relationships that could be construed as a potential conflict of interest.

Publisher's note

All claims expressed in this article are solely those of the authors and do not necessarily represent those of their affiliated organizations, or those of the publisher, the editors and the reviewers. Any product that may be evaluated in this article, or claim that may be made by its manufacturer, is not guaranteed or endorsed by the publisher.

Supplementary material

The Supplementary Material for this article can be found online at: https://www.frontiersin.org/articles/10.3389/feart.2024. 1354185/full#supplementary-material

SUPPLEMENTARY FIGURE S1:
Plots of FeOT, MgO, TiO2, P2O5, Na2O, K2O, Nb, Sr, Rb, Ba, La, and Th versus LOI for the studied granites studied.

References

Andersen, T. (2002). Correction of common lead in U–Pb analyses that do not report 204Pb. *Chem. Geol.* 192, 59–79. doi:10.1016/s0009-2541(02)00195-x

Ballouard, C., Poujol, M., Boulvais, P., Branquet, Y., Tartèse, R., and Vigneresse, J. L. (2016). Nb-Ta fractionation in peraluminous granites: a marker of the magmatic-hydrothermal transition. *Geology* 44, 231–234. doi:10.1130/g37475.1

Brown, M. (2013). Granite: from genesis to emplacement. *Geol. Soc. Am. Bull.* 125, 1079–1113. doi:10.1130/b30877.1

Campbell, I. H., and Taylor, S. R. (1983). No water, no granites - No oceans, no continents. *Geophys. Res. Lett.* 10, 1061–1064. doi:10.1029/gl010i011p01061

Chappell, B. W., and White, A. J. R. (1974). Two contrasting granite types. *Pac. Geol.* 8, 173–174.

Chen, G., Hu, F., Robertson, A. H., Garzanti, E., Zhang, S., and Wu, F. Y. (2023). A combined methodology for reconstructing source-to-sink basin evolution, exemplified by the Triassic Songpan–Ganzi basin, central China. *Sediment. Geol.* 458, 106529. doi:10.1016/j.sedgeo.2023.106529

Chen, J. Y., Yang, J. H., Zhang, J. H., Sun, J. F., Zhu, Y. S., and Hartung, E. (2021). Generation of Cretaceous high-silica granite by complementary crystal accumulation and silicic melt extraction in the coastal region of southeastern China. *GSA Bull.* 134, 201–222. doi:10.1130/b35745.1

Clemens, J. D., and Stevens, G. (2012). What controls chemical variation in granitic magmas? *Lithos* 134-135, 317–329. doi:10.1016/j.lithos.2012.01.001

Deng, G., Jiang, D., Zhang, R., Huang, J., Zhang, X., and Huang, F. (2022). Barium isotopes reveal the role of deep magmatic fluids in magmatic-hydrothermal evolution and tin enrichment in granites. *Earth Planet. Sci. Lett.* 117724, 594.

DePaolo, D. J. (1988). Age dependence of the composition of continental crust: evidence from Nd isotopic variations in granitic rocks. *Earth Planet. Sci. Lett.* 90, 263–271. doi:10.1016/0012-821x(88)90130-6

de Sigoyer, J., Vanderhaeghe, O., Duchêne, S., and Billerot, A. (2014). Generation and emplacement of Triassic granitoids within the Songpan Ganze accretionary-orogenic wedge in a context of slab retreat accommodated by tear faulting, Eastern Tibetan plateau, China. *J. Asian Earth Sci.* 88, 192–216. doi:10.1016/j.jseaes.2014.01.010

Ding, L., Yang, D., Cai, F. L., Pullen, A., Kapp, P., Gehrels, G. E., et al. (2013). Provenance analysis of the mesozoic hoh-xil-songpan-ganzi turbidites in northern tibet: implications for the tectonic evolution of the eastern paleo-tethys ocean. *Tectonics* 32, 34–48. doi:10.1002/tect.20013

Ferry, J. M., and Watson, E. B. (2007). New thermodynamic models and revised calibrations for the Ti-in-zircon and Zr-in-rutile thermometers. *Contributions Mineralogy Petrology* 154, 429–437. doi:10.1007/s00410-007-0201-0

Frost, B., Barnes, C., Collins, W., Arculus, R., Ellis, D., and Frost, C. (2001). A geochemical classification for granitic rocks. *J. Petrology* 42, 2033–2048. doi:10.1093/petrology/42.11.2033

Frost, C. D., Swapp, S. M., Frost, B. R., Finley-Blasi, L., and Fitz-Gerald, D. B. (2016). Leucogranites of the teton range, Wyoming: a record of archean collisional orogeny. *Geochimica Cosmochimica Acta* 185, 528–549. doi:10.1016/j.gca.2015.12.015

Gao, L. E., Zeng, L. S., and Asimow, P. D. (2017). Contrasting geochemical signatures of fluid-absent versus fluid-fluxed melting of muscovite in metasedimentary sources: the Himalayan leucogranites. *Geology* 45, 39–42. doi:10.1130/g38336.1

Gao, P., Zheng, Y. F., and Zhao, Z. F. (2016). Experimental melts from crustal rocks: a lithochemical constraint on granite petrogenesis. *Lithos* 266-267, 133–157. doi:10.1016/j.lithos.2016.10.005

Glazner, A. F. (2014). Magmatic life at low Reynolds number. *Geology* 42, 935–938. doi:10.1130/g36078.1

Glazner, A. F., Coleman, D. S., and Bartley, J. M. (2008). The tenuous connection between high-silica rhyolites and granodiorite plutons. *Geology* 36, 183. doi:10.1130/g24496a.1

Harris, N. B. W., and Inger, S. (1992). Trace element modelling of pelite-derived granites. *Contributions Mineralogy Petrology* 110, 46–56. doi:10.1007/bf00310881

He, S. P., Li, R. S., Wang, C., Gu, P. Y., Shi, C., and Zha, X. F. (2013). Reaseach on the formation age of Ningduo rock group in Changdu block: evidence for the existence of basement in the North Qiangtang. *Earth Sci. Front.* 20, 15–24.

Hoskin, P. W. O. (2005). Trace-element composition of hydrothermal zircon and the alteration of Hadean zircon from the Jack Hills, Australia. *Geochimica Cosmochimica Acta* 69, 637–648. doi:10.1016/j.gca.2004.07.006

Hoskin, P. W. O., and Schaltegger, U. (2003). The composition of zircon and igneous and metamorphic petrogenesis. *Rev. Mineralogy Geochem.* 53, 27–62. doi:10.2113/0530027

Inger, S., and Harris, N. (1993). Geochemical constraints on leucogranite magmatism in the langtang valley, Nepal Himalaya. *J. Petrology* 34, 345–368. doi:10.1093/petrology/34.2.345

Irvine, T. N., and Baragar, W. R. A. (1971). A guide to the chemical classification of the common volcanic rocks. *Can. J. Earth Sci.* 8, 523–548. doi:10.1139/e71-055

Jian, X., Weislogel, A., and Pullen, A. (2019). Triassic sedimentary filling and closure of the eastern paleo-Tethys Ocean: new insights from detrital zircon geochronology of Songpan-Ganzi, Yidun, and west Qinling flysch in eastern Tibet. *Tectonics* 38 (2), 767–787. doi:10.1029/2018tc005300

Keller, C. B., Schoene, B., Barboni, M., Samperton, K. M., and Husson, J. M. (2015). Volcanic–plutonic parity and the differentiation of the continental crust. *Nature* 523, 301–307. doi:10.1038/nature14584

King, P. L., White, A. J. R., Chappell, B. W., and Allen, C. M. (1997). Characterization and origin of aluminous A-type granites from the Lachlan Fold Belt, southeastern Australia. *J. Petrology* 38, 371–391. doi:10.1093/petroj/38.3.371

Lee, C. T. A., and Morton, D. M. (2015). High silica granites: terminal porosity and crystal settling in shallow magma chambers. *Earth Planet. Sci. Lett.* 409, 23–31. doi:10.1016/j.epsl.2014.10.040

Liu, B., Ma, C. Q., Guo, Y. H., Xiong, F. H., Guo, P., and Zhang, X. (2016a). Petrogenesis and tectonic implications of Triassic mafic complexes with MORB/OIB affinities from the western Garzê-Litang ophiolitic mélange, central Tibetan Plateau. *Lithos* 260, 253–267. doi:10.1016/j.lithos.2016.06.009

Liu, B., Ma, C. Q., Huang, J., Xiong, F. H., Zhang, X., and Guo, Y. H. (2016b). Petrogenetic mechanism and tectonic significance of Triassic Yushu volcanic rocks in the northern part of the North Qiangtang Terrane. *Acta Petrologica Mineralogica* 35, 1–15.

Liu, B., Ma, C. Q., Tang, Y. J., Dong, H., Xu, Y., Zhao, S. Q., et al. (2021). Triassic high-Mg andesitic magmatism induced by sediment melt-peridotite interactions in the central Tibetan Plateau. *Lithos* 106266, 398–399.

Liu, B., Tang, Y. J., Xing, L. Y., Xu, Y., Zhao, S. Q., Sun, Y., et al. (2022). Triassic calc-alkaline lamprophyre dykes from the North Qiangtang, central Tibetan Plateau: evidence for a subduction-modified lithospheric mantle. *Geol. Mag.* 159 (3), 407–420. doi:10.1017/s001675682100100x

Liu, B., Xu, Y., Li, Q., Sun, Y., Zhao, S. Q., Huang, J., et al. (2020). Origin of Triassic mafic magmatism in the North Qiangtang terrane, central Tibetan Plateau: implications for the development of a continental back-arc basin. *J. Geol. Soc.* 177, 826–842. doi:10.1144/jgs2019-130

Liu, B., Xu, Y., Ma, C. Q., Li, F. L., Zhao, S. Q., Zhan, J. M., et al. (2023). Petrogenesis and geodynamic setting of the ningduo peraluminous granites from the North Qiangtang terrane. *Earth Sci.*, 1–32.

Liu, Y., Xiao, W. J., Windley, B. F., Li, R. S., Ji, W. H., Zhou, K. F., et al. (2019). Late Triassic ridge subduction of Paleotethys: insights from high-Mg granitoids in the Songpan-Ganzi area of northern Tibet. *Lithos* 334-335, 254–272. doi:10.1016/j.lithos.2019.03.012

Liu, Y. S., Gao, S., Hu, Z. C., Gao, C. G., Zong, K. Q., and Wang, D. B. (2010). Continental and oceanic crust recycling-induced melt-peridotite interactions in the trans-north China orogen: U-Pb dating, Hf isotopes and trace elements in zircons from mantle xenoliths. *J. Petrology* 51, 537–571. doi:10.1093/petrology/egp082

Liu, Y. S., Zong, K. Q., Kelemen, P. B., and Gao, S. (2008). Geochemistry and magmatic history of eclogites and ultramafic rocks from the Chinese continental scientific drill hole: subduction and ultrahigh-pressure metamorphism of lower crustal cumulates. *Chem. Geol.* 247, 133–153. doi:10.1016/j.chemgeo.2007.10.016

Maniar, P. D., and Piccoli, P. M. (1989). Tectonic discrimination of granitoids. *Geol. Soc. Am. Bull.* 101, 635–643. doi:10.1130/0016-7606(1989)101<0635:tdog>2.3.co;2

McDonough, W. F., and Sun, S. S. (1995). The composition of the Earth. *Chem. Geol.* 120, 223–253. doi:10.1016/0009-2541(94)00140-4

Middlemost, E. A. K. (1994). Naming materials in the magma/igneous rock system. *Earth-Science Rev.* 37, 215–224. doi:10.1016/0012-8252(94)90029-9

Miller, C. F., McDowell, S. M., and Mapes, R. W. (2003). Hot and cold granites? Implications of zircon saturation temperatures and preservation of inheritance. *Geology* 31, 529. doi:10.1130/0091-7613(2003)031<0529:hacgio>2.0.co;2

Patiño Douce, A. E., and Harris, N. (1998). Experimental constraints on himalayan anatexis. *J. Petrology* 39, 689–710. doi:10.1093/petrology/39.4.689

Peccerillo, A., and Taylor, S. R. (1976). Geochemistry of eocene calc-alkaline volcanic rocks from the Kastamonu area, Northern Turkey. *Contributions Mineralogy Petrology* 58, 63–81. doi:10.1007/bf00384745

Roger, F., Arnaud, N., Gilder, S., Tapponnier, P., Jolivet, M., Brunel, M., et al. (2003). Geochronological and geochemical constraints on Mesozoic suturing in east central Tibet. *Tectonics* 22. doi:10.1029/2002tc001466

Saito, S., Arima, M., Nakajima, T., and Kimura, J. I. (2004). Petrogenesis of Ashigawa and Tonogi granitic intrusions, southern part of the Miocene Kofu Granitic Complex, central Japan: M-type granite in the Izu arc collision zone. *J. Mineralogical Petrological Sci.* 99, 104–117. doi:10.2465/jmps.99.104

Schiller, D., and Finger, F. (2019). Application of Ti-in-zircon thermometry to granite studies: problems and possible solutions. *Contributions Mineralogy Petrology* 174, 51. doi:10.1007/s00410-019-1585-3

She, Z., Ma, C., Mason, R., Li, J., Wang, G., and Lei, Y. (2006). Provenance of the triassic songpan–ganzi flysch, west China. *Chem. Geol.* 231, 159–175. doi:10.1016/j.chemgeo.2006.01.001

Shuai, X., Li, S. M., Zhu, D. C., Wang, Q., Zhang, L. L., and Zhao, Z. D. (2021). Tetrad effect of rare earth elements caused by fractional crystallization in high-silica granites: an example from central Tibet. *Lithos* 384–385.

Song, P. P., Ding, L., Li, Z. Y., Lippert, P. C., Yang, T. S., Zhao, X. X., et al. (2015). Late triassic paleolatitude of the Qiangtang block: implications for the closure of the paleo-tethys ocean. *Earth Planet. Sci. Lett.* 424, 69–83. doi:10.1016/j.epsl.2015.05.020

Sun, S. S., and McDonough, W. F. (1989). Chemical and isotopic systematics of oceanic basalts: implications for mantle composition and processes. *Geol. Soc. Spec. Publ.* 42, 313–345.

Tan, J., Wei, J. H., Zhao, S. Q., Li, Y. J., Liu, Y., Liu, X. Y., et al. (2020). Petrogenesis of Late Triassic high-Mg diorites and associated granitoids with implications for Paleo-Tethys evolution in the northeast Tibetan Plateau. *GSA Bull.* 132, 955–976. doi:10.1130/b35225.1

Tao, Y., Bi, X. W., Li, C. S., Hu, R. Z., Li, Y. B., and Liao, M. Y. (2014). Geochronology, petrogenesis and tectonic significance of the Jitang granitic pluton in eastern Tibet, SW China. *Lithos* 184-187, 314–323. doi:10.1016/j.lithos.2013.10.031

Taylor, S. R., and McLennan, S. M. (1985). *The continental crust: its composition and evolution. An examination of the geochemical record preserved in sedimentary rocks*. Oxford: Blackwell Scientific Publications, 328.

Wang, Q., Wyman, D. A., Xu, J., Wan, Y., Li, C., Zi, F., et al. (2008). Triassic Nb-enriched basalts, magnesian andesites, and adakites of the Qiangtang terrane (Central Tibet): evidence for metasomatism by slab-derived melts in the mantle wedge. *Contributions Mineralogy Petrology* 155, 473–490. doi:10.1007/s00410-007-0253-1

Wang, Z. L. (2009). *Study of multiple orogeny and metallogenesis inYushu area, northern segment of sanjiang*. Beijing: Chinese Academy of Geological Sciences, 122.

Weinberg, R. F., and Hasalová, P. (2015). Water-fluxed melting of the continental crust: a review. *Lithos* 212-215, 158–188. doi:10.1016/j.lithos.2014.08.021

Weislogel, A. L., Graham, S. A., Chang, E. Z., Wooden, J. L., Gehrels, G. E., and Yang, H. (2006). Detrital zircon provenance of the late triassic songpan-ganzi complex: sedimentary record of collision of the North and south China blocks. *Geology* 34 (2), 97–100. doi:10.1130/g21929.1

Whalen, J. B., Currie, K. L., and Chappell, B. W. (1987). A-type granites: geochemical characteristics, discrimination and petrogenesis. *Contributions Mineralogy Petrology* 95, 407–419. doi:10.1007/bf00402202

Wu, F. Y., Liu, X. C., Ji, W. Q., Wang, J. M., and Yang, L. (2017). Highly fractionated granites: recognition and research. *Sci. China Earth Sci.* 60, 1201–1219. doi:10.1007/s11430-016-5139-1

Wu, F. Y., Liu, X. C., Liu, Z. C., Wang, R. C., Xie, L., Wang, J. M., et al. (2020). Highly fractionated Himalayan leucogranites and associated rare-metal mineralization. *Lithos*, 352–353.

Xu, Z., Dilek, Y., Cao, H., Yang, J., Robinson, P., Ma, C., et al. (2015). Paleo-tethyan evolution of tibet as recorded in the east cimmerides and west cathaysides. *J. Asian Earth Sci.* 105, 320–337. doi:10.1016/j.jseaes.2015.01.021

Yang, T. N., Hou, Z. Q., Wang, Y., Zhang, H. R., and Wang, Z. L. (2012). Late paleozoic to early mesozoic tectonic evolution of northeast tibet: evidence from the triassic composite western jinsha-garzê-litang suture. *Tectonics* 31. doi:10.1029/2011tc003044

Yuan, C., Zhou, M. F., Sun, M., Zhao, Y. J., Wilde, S., Long, X. P., et al. (2010). Triassic granitoids in the eastern Songpan Ganzi Fold Belt, SW China: magmatic response to geodynamics of the deep lithosphere. *Earth Planet. Sci. Lett.* 290, 481–492. doi:10.1016/j.epsl.2010.01.005

Zeng, L. S., and Gao, L. E. (2017). Cenozoic crustal anatexis and the leucogranites in the Himalayan collisional orogenic belt. *Acta Petrol. Sin.* 33 (5), 1420–1444.

Zhang, H. F., Parrish, R., Zhang, L., Xu, W. C., Yuan, H. L., Gao, S., et al. (2007). A-type granite and adakitic magmatism association in Songpan–Garze fold belt, eastern Tibetan Plateau: implication for lithospheric delamination. *Lithos* 97, 323–335. doi:10.1016/j.lithos.2007.01.002

Zhang, H. R., Yang, T. N., Hou, Z. Q., Song, Y. C., Cheng, X. F., Ding, Y., et al. (2013). Chronology and geochemistry of mylonitic quartz diorites in the Yushu melange, central Tibet. *Acta Petrol. Sin.* 29, 3871–3882.

Zhang, K. J., Li, B., and Wei, Q. G. (2012). Diversified provenance of the songpan-ganzi triassic turbidites, Central China: constraints from geochemistry and Nd isotopes. *J. Geol.* 120, 69–82. doi:10.1086/662716

Zhao, H., Chen, B., Huang, C., Bao, C., Yang, Q., and Cao, R. (2022). Geochemical and Sr–Nd–Li isotopic constraints on the genesis of the Jiajika Li-rich pegmatites, eastern Tibetan Plateau: implications for Li mineralization. *Contributions Mineralogy Petrology* 177 (1), 4. doi:10.1007/s00410-021-01869-3

Zhao, S. Q., Tan, J., Wei, J. H., Tian, N., Zhang, D. H., Liang, S. N., et al. (2014). Late Triassic Batang Group arc volcanic rocks in the northeastern margin of Qiangtang terrane, northern Tibet: partial melting of juvenile crust and implications for Paleo-Tethys ocean subduction. *Int. J. Earth Sci.* 104, 369–387. doi:10.1007/s00531-014-1080-z

Zhu, R. Z., Lai, S. C., Fowler, M., Xie, J. C., and Glynn, S. M. (2023). A microcosm of modern crust formation: evidence from zircon ages, Hf O and Nd Sr isotopes and bulk geochemistry of the Menglian Batholith, SE Tibet. *Chem. Geol.*, 618.